Published in final edited form as:

Cell Rep. 2020 July 07; 32(1): 107845. doi:10.1016/j.celrep.2020.107845.

Kinetic Heterogeneity of Cancer Cell Fractional Killing

Zintis Inde[1], **Giovanni C. Forcina**[1], **Kyle Denton**[1], **Scott J. Dixon**[1,2,*]

[1]Department of Biology, Stanford University, Stanford, CA 94305, USA

[2]Lead Contact

SUMMARY

Lethal drugs can induce incomplete cell death in a population of cancer cells, a phenomenon referred to as fractional killing. Here, we show that high-throughput population-level time-lapse imaging can be used to quantify fractional killing in response to hundreds of different drug treatments in parallel. We find that stable intermediate levels of fractional killing are uncommon, with many drug treatments resulting in complete or near-complete eradication of all cells, if given enough time. The kinetics of fractional killing over time vary substantially as a function of drug, drug dose, and genetic background. At the molecular level, the antiapoptotic protein MCL1 is an important determinant of the kinetics of fractional killing in response to MAPK pathway inhibitors but not other lethal stimuli. These studies suggest that fractional killing is governed by diverse lethal stimulus-specific mechanisms.

Graphical Abstract

*Correspondence: sjdixon@stanford.edu.

AUTHOR CONTRIBUTIONS

Conceptualization, Z.I., G.C.F., and S.J.D.; Methodology, Z.I. and G.C.F.; Investigation, Z.I., G.C.F., and K.D.; Writing – Original Draft, Z.I. and S.J.D.; Writing – Review & Editing, Z.I., G.C.F., and S.J.D.; Funding Acquisition and Supervision, S.J.D.

DECLARATION OF INTERESTS

S.J.D. is a member of the scientific advisory board of Ferro Therapeutics and is a consultant for Toray Industries.

SUPPLEMENTAL INFORMATION

Supplemental Information can be found online at https://doi.org/10.1016/j.celrep.2020.107845.

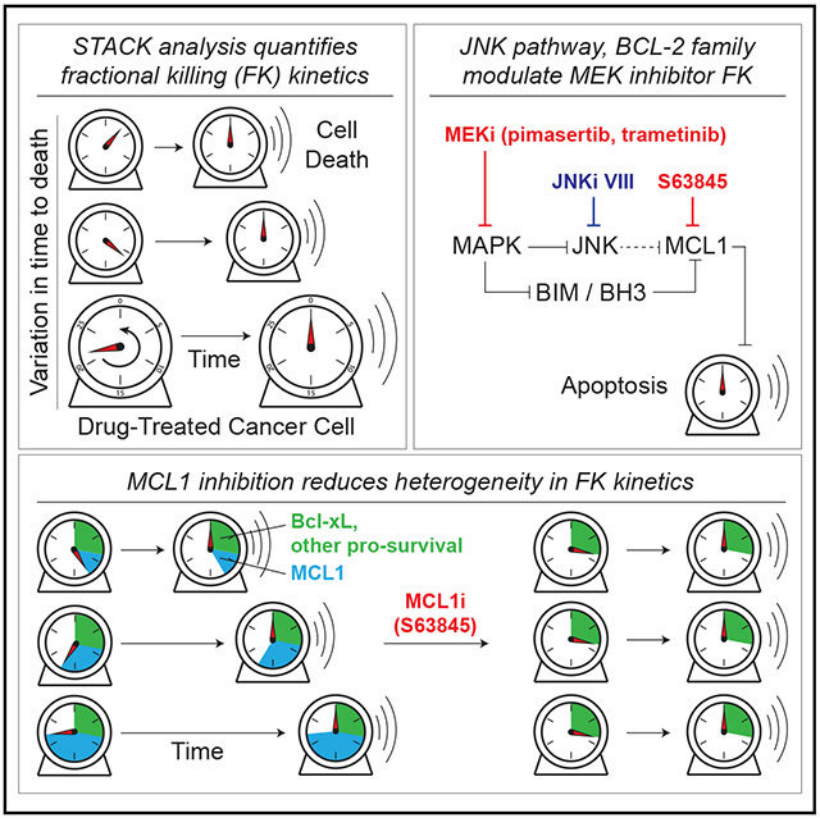

In Brief

Anticancer drugs typically kill only a fraction of cells within a population at a given time. Inde et al. develop high-throughput methods to quantify fractional killing in hundreds of populations in parallel and find that the molecular mechanisms regulating this phenomenon are likely to be diverse.

INTRODUCTION

Individual cells within a population can exhibit remarkable variability in their responses to lethal drugs that cannot be explained by the presence of genetic differences (Bigger, 1944; Shaffer et al., 2017; Spencer et al., 2009). For example, rare drug-tolerant persister cells can survive in the presence of drug for many weeks and subsequently give rise to both drug-sensitive and drug-tolerant progeny when the drug is removed (Raha et al., 2014; Sharma et al., 2010). Over shorter timescales, drugs can be titrated to kill half the cells within a population, leaving the other half alive (Figure 1A). This variability in cell death within a population may be explained by differences in drug uptake or target protein expression and engagement (Lu et al., 2018; Mateus et al., 2017). However, even at saturating doses, many drugs do not kill all cells within a population, at least at a given time point (Fallahi-Sichani et al., 2013; Wolpaw et al., 2011). The nature of this cell-to-cell variability in drug responsiveness is of substantial fundamental and translational interest.

In cancer patients, variability between cells in drug-induced cell death can manifest as "fractional killing'' (FK), whereby a constant fraction of tumor cells are killed in response to each cycle of drug administration (Berenbaum, 1972; Roux et al., 2015). The molecular origins of FK remain poorly understood but, in addition to differences in target inhibition, can involve nongenetic differences between cells in caspase activity, p53 expression, c-Jun N-terminal kinase (JNK) pathway activity, and mitochondrial abundance (Miura et al., 2018; Paek et al., 2016; Roux et al., 2015; Santos et al., 2019; Shaffer et al., 2017; Spencer et al., 2009). Whether these different mechanisms contribute to FK in response to all lethal stimuli is not clear.

Existing studies of FK *in vitro* have generally focused on one or a limited number of lethal conditions at a time, in part due to the perceived need to track the fate of each individual cell within a population over time (Miura et al., 2018; Paek et al., 2016; Roux et al., 2015). This technical limitation has prevented larger-scale comparative studies of how FK varies between drugs, drug doses, and genetic backgrounds. Here, we show that it is possible to assess FK in hundreds of cancer cell populations in parallel using the scalable time-lapse analysis of cell death kinetics (STACK) method (Forcina et al., 2017). In this method, the fate of individual cells is not tracked directly. Rather, the total number of live and dead cells within a population is counted repeatedly over time. This approach eliminates the data acquisition bottleneck associated with tracking individual cell fates, while retaining the ability to capture overall population fractional killing.

Using this approach, we find that FK can vary substantially between lethal compounds and compound doses in the same genetic background, and for the same lethal compound between genetic backgrounds. Substantial differences in the rate of FK over time are apparent between lethal conditions, which is independent of the total degree of FK within a population by the end of a treatment period. As a case study, we examine FK in response to inhibitors of the mitogen-activated protein kinase (MAPK) cascade and find that the antiapoptotic protein MCL1 is one important regulator of the rate of FK in response to inhibitors of this pathway but not other lethal stimuli. Our results demonstrate that it is possible to analyze FK in a high-throughput manner and suggest that this phenomenon is governed by diverse molecular mechanisms.

RESULTS

High-Throughput Analysis of Fractional Killing Using STACK

Our initial goal was to determine how FK varied between lethal compounds, compound doses, and genetic backgrounds. Using the STACK method, we generated a test dataset for populations of genetically distinct T98G^{N} glioblastoma and U-2 OS^{N} osteosarcoma cells treated with a single administration of 10 mechanistically distinct lethal compounds, each in a 10-point, 2-fold dose-response series. Individual live cells are marked by stable expression of nuclear-localized mKate2 (denoted by the superscript "N" next to the cell line name), and dead cells are identified by uptake of the normally membrane-impermeant dye SYTOX Green. We counted live and dead cells for all 200 populations in parallel every 2 h for a total of 120 h. From these counts, we computed the lethal fraction at each timepoint, where a score of 0 means all cells within the population are alive and a score of 1 means all cells are

dead (Figure 1B). Lethal fraction scores therefore represent an instantaneous measure of FK within the population at any given time. These data were initially visualized as heatmaps of lethal fraction scores over time for each drug and drug concentration (Figures 1C and S1A).

We first explored how FK varied as a function of compound concentration. We initially hypothesized that through titration we could achieve a graded and stable degree of FK in different populations. However, contrary to this hypothesis, stable intermediate levels of FK were not always observed. For proapoptotic compounds like the proteasome inhibitor MG132 and the sarco-endoplasmic reticulum Ca^{2+} ATPase inhibitor thapsigargin, as well as for compounds that induce nonapoptotic cell death such as the system x_c^- inhibitor erastin and the glutathione peroxidase 4 inhibitor ML162, different compound concentrations tended to produce either high levels of FK, with the maximum lethal fraction (LF_{max}) approaching 1, or little FK, with LF_{max} remaining near 0 (Figures 1D, S1B, and S1C). The boundaries between high and low FK often spanned as little as a 4-fold concentration range. Some concentrations of the topoisomerase inhibitors etoposide and camptothecin, and the microtubule poisons paclitaxel and vinblastine, did produce a more intermediate level of FK during the observation period. However, this may be simply because these compounds take longer to kill cells. Thus, FK tends toward high levels once a minimum compound concentration threshold is exceeded.

The classic understanding of FK relates to the total amount of cell death within the population. While generally high levels of FK were common, we were curious whether complete eradication of all live cells was typical or whether there always remained some subpopulation of surviving cells (e.g., persisters) (Figure 1E). In $T98G^N$ cells, most compounds achieved >95% FK (i.e., $LF_{max} > 0.95$), with three achieving >99% FK, by 120 h. In U-2 OS^N cells, fewer compounds caused greater than 95% FK by 120 h. Live cells remaining at 120 h could represent stable drug-tolerant subpopulations. If so, however, these populations were small and variable in size, and therefore appeared unlikely to be explained by a single generalizable compound tolerance mechanism.

Given that most lethal treatments examined here ultimately produced high levels of FK, we searched for differences in how FK manifested over time. One possibility was that all cells within the population would die at roughly the same time in response to a given lethal treatment. An alternative possibility was that the initiation of cell death would vary substantially between cells. Notably, even at the highest tested compound concentrations, substantial differences were apparent in the time between early and late cell deaths within each population. To quantify this, we computed the span of time between when the lethal fraction score first exceeded 0.25 and then 0.75 (Figure 1G). In $T98G^N$ cells, this span ranged from 10 h (staurosporine) to 64 h (vinblastine), with a median of 30 h across all compounds. These death spans did not correlate with the time points of global cell death initiation within the population and were not necessarily explained by differences in the overall lethality of a given compound. For example, in $T98G^N$ cells and to a lesser extent U-2 OS^N cells, the death spans for ML162, etoposide, thapsigargin, and paclitaxel varied substantially despite similar overall levels of FK by 120 h (Figure 1G). For the remainder of this work, we focused mainly on such differences in the kinetics of FK over time.

Quantifying Fractional Killing Kinetics

The death span measurement provided an initial characterization of the variability in the onset of cell death between individual cells in a population. However, to more easily compare the kinetics of FK between conditions, we sought metrics that were easier to compute and compare. We showed previously that lethal fraction scores over time can be fitted with a lag exponential death (LED) model that allows for the extraction of two key parameter values describing cell death within the population: D_O and D_R (Figure 2A) (Forcina et al., 2017). D_O reflects the time when cells within the population begin to die in large numbers. By contrast, D_R captures the maximal rate of cell death within the population (i.e., the maximum slope of the lethal fraction curve at D_O), expressed here as a percentage over time (% h^{-1}). We realized that D_R could be used to summarize the kinetics of FK within the population: high D_R values indicate that cells die more synchronously over time, while low D_R values indicate that cells die more asynchronously (Figure 2B).

We next investigated how D_R varied for a subset of the lethal conditions examined above in U-2 OS^N and $T98G^N$ cells. While D_R varied between lethal compounds, it rarely exceeded 6% h^{-1} and in most cases was below 3% h^{-1}, even at the highest tested compound concentrations (Figure 2C). These D_R values suggest that individual cells within the population undergo the terminal phase of cell death (i.e., membrane permeabilization) at different times, a phenotype we confirmed by visual inspection (Figures 2D, S2A, and S2B). Interestingly, D_R values varied little over several orders of magnitude of compound concentration. Thus, for these lethal compounds, the maximal rate of FK within the population is generally insensitive to the amount of lethal stimulus once a certain threshold is exceeded. This may be consistent with the observation that FK tends to proceed to completion in response to most conditions that produce some degree of lethality. This also indicates that there are fundamental constraints on the rate of FK.

Having examined the kinetics of FK across doses and between cell lines for a limited number of lethal compounds, we next wished to survey more broadly the range of FK kinetics that were observable in cancer cells. Toward this end, we examined how FK varied between 140 mechanistically diverse lethal compounds previously tested in U-2 OS osteosarcoma cells at a single dose of 5 μM for 120 h (Figure 2E) (Forcina et al., 2017). 139 of 140 compounds yielded lethal fraction scores over time where it was possible to determine D_R values. Across all compounds, median D_R was 2.4% h^{-1} (1.6%–4.6% h^{-1} interquartile range) (Figure 2F), consistent with our analysis of a more limited set of lethal compounds above. Most compounds in this set have a specific molecular target, which allowed us to ask how the kinetics of FK varied by compound target. Interestingly, different proteasome inhibitors and histone deacetylase (HDAC) inhibitors consistently triggered relatively faster FK (median D_R > 5% h^{-1}) than inhibitors of cyclin-dependent kinases (CDK), microtubule function, and mitogen-activated protein kinase kinase 1 and 2 (MEK1/2) (median D_R < 2% h^{-1}) (Figures 2G and 2H). Thus, the rate of FK within a population over time can vary substantially between lethal compounds with distinct targets.

MEKis Trigger FK with Slow Kinetics

We hypothesized that molecular differences between cells within a population would account for the observed variation in FK over time. To explore this hypothesis, we focused on the effects of MEK1/2 inhibitors (MEKis), which block the function of the RAS/MAPK signal transduction pathway, and triggered FK with slow kinetics in our retrospective analysis of U-2 OS cells (Figures 2G and 3A). We first examined whether slow MEKi-induced FK was generalizable to other cell lines or targets in the MAPK pathway, and whether molecular mechanisms that govern this slow FK also impacted FK in response to lethal stimuli targeting other pathways. MEKis are being investigated for use in the treatment of various cancers including lung cancer (Kim and Giaccone, 2018). We therefore initially pursued our follow-on studies using non-small cell lung carcinoma (NSCLC) models. Confirming the results of the large-scale screen, the structurally distinct MEKis pimasertib (Pim) and trametinib (Tram) both triggered slow FK ($D_R < 3\%\ h^{-1}$) across a range of lethal concentrations in three different KRAS mutant NSCLC cell lines, A549, Calu-6, and H2291, consistent with a broadly generalizable FK phenotype (Figures 3B, 3C, and S3A).

The slow kinetics of MEKi-induced FK made it difficult to assess in the above experiments whether incomplete cell death in the population at the end of one week reflected the existence of an inherently drug-tolerant subpopulation or simply that the lethal process had not yet gone to completion. To investigate, we performed longer-term dose-response studies over 2 weeks in $A549^N$ cells (Figure S3B). Consistent with our observations of $T98G^N$ and U-2 OS^N cells treated with different lethal molecules (Figures 1C, 1D, and S1A), only a single Pim concentration (2.5 μM) produced an intermediate level of FK that was stable over 2 weeks. Lower doses were largely not lethal, while Pim treatment of 5 μM or more resulted in $LF_{max} \geq 0.93$ by the end of 2 weeks, with 20 μM Pim resulting in $LF_{max} = 0.99 \pm 0.01$. Thus, the slow rate of cell death triggered by Pim treatment can nonetheless yield essentially complete FK if given enough time. The small numbers of live cells remaining after 2 weeks of Pim treatment at 5 μM or higher concentrations could represent drug-tolerant cells of some kind, but this was not investigated further here. Since measurements over 14 days were technically challenging, going forward, we used the lowest doses of Pim (5 μM) and Tram (500 nM) that triggered consistently high levels of FK (lethal fraction ~0.7) in $A549^N$ cells by 120 h for most experiments.

A trivial explanation for FK is variable inhibition of the drug target. However, phosphorylation of the MEK1/2 substrates ERK1/2 was fully inhibited by Pim in as little as 2 h, long before the initiation of cell death, with a lethal concentration (i.e., 5 μM) causing sustained inhibition of ERK1/2 phosphorylation over 48 h (Figures 3D and 3E). Using the single-cell ERK kinase translocation reporter (KTR) (Regot et al., 2014), we also found that lethal MEKi treatment resulted in greater reporter nuclear translocation before the onset of cell death than nonlethal MEKi treatment or lethal control (i.e., bortezomib) treatment (Figure 3F). Thus, differential inhibition of ERK1/2 phosphorylation did not explain slow FK in response to MEKis.

We next sought to identify proteins or processes downstream of MEK1/2 that could mediate slow FK. Similar to MEKis, direct inhibition of ERK1/2 using the small-molecule ERK1/2

inhibitor (ERKi) SCH772984 resulted in slow FK in both $A549^N$ and Calu-6^N cells (Figures 3G and S3C). We confirmed that SCH772984 effectively reduced expression of DUSP4, a target of the MAPK pathway, at both 2 and 48 h (Figures 3H and 3I). The similar MEK1/2i and ERKi phenotypes argued against the existence of an inherently drug-resistant (i.e., mutant) subpopulation. Indeed, Pim triggered FK with similar kinetics in both drug-naive cells and cells that survived an initial round of MEKi treatment (Figure 3J). Rather, we hypothesized that slow FK was due to nongenetic variation at the molecular level acting downstream or in parallel to ERK1/2. Several known candidate mechanisms of FK(lnde and Dixon, 2018), including p53 expression, differences in glycolytic or oxidative metabolism, or reactive oxygen species (ROS) accumulation, did not modulate MEKi-induced FK (Figures S3D-S3K). Thus, the molecular variability contributing to FK in response to MAPK pathway inhibition appeared to reside elsewhere in the molecular network.

Variable MCL1 Expression Contributes to Slow FK

How inhibition of the MAPK pathway induced FK with slow kinetics remained unclear. To explore this question further, we pursued a series of mechanistic investigations. Testing the role of protein synthesis, we found that MEKi-induced cell death was potently suppressed by co-treatment with cycloheximide, suggesting that the translation of certain gene products was necessary for cell death (Figure S4A). Using RNA sequencing (RNA-seq), we identified a set of 555 genes significantly upregulated by lethal (i.e., 5 μM) Pim treatment in both $A549^N$ and Calu-6^N cells, but not by a cytostatic Pim treatment (0.5 μM), that was enriched for regulators of apoptosis (Figures 4A and 4B). In line with the induction of apoptosis, cell death induced by MEKis or the positive control bortezomib was suppressed by co-treatment with the pan-caspase inhibitor Q-VD-OPh (Figure S4B). The MAPK pathway can regulate apoptosis (Cragg et al., 2008; Hata et al., 2014; Meng et al., 2010), and variable expression of apoptotic proteins is linked to FK in other contexts (Roux et al., 2015). Accordingly, we focused on how key apoptotic proteins impacted FK in response to MEKis.

Based on literature precedent, we first examined the roles of the proapoptotic BH3-only protein BIM and the antiapoptotic protein BCL-xL (Cragg et al., 2008; Hata et al., 2014; Meng et al., 2010). As expected, BIM levels increased, and BCL-xL levels decreased, following MEKi treatment in both $A549^N$ and Calu-6^N cells (Figure S4C). The increase in BIM levels in response to Pim treatment was blocked by cycloheximide, consistent with BIM upregulation promoting cell death (Figure S4D). We reasoned that if slow FK was due to variable expression of either BIM or BCL-xL between cells, then equalizing protein expression or function between cells by BIM overexpression or BCL-xL inhibition should tend to “synchronize” cell death within the population, resulting in higher D_R values in response to MEKi treatment. Doxycycline (Dox)-inducible overexpression of wild-type BIM, but not inactive BIM^{G156E} (Marani et al., 2002), did shorten the time to cell death onset (i.e., D_O) but did not alter D_R in response to MEKis, across a range of tested Dox doses (Figure S4E-S4I). Likewise, co-treatment of $A549^N$ cells with the BCL-xL/BCL-2 inhibitor ABT-737 or the BCL-xL-selective inhibitor A-1155463 shortened D_O without increasing D_R (Figures 4C–4E). Thus, BIM and BCL-xL helped set the threshold for MEKi-induced cell death but were not primary regulators of the rate of FK in response to MEK1/2 inhibition.

In addition to BCL-xL, the antiapoptotic protein MCL1 can also regulate apoptosis in response to inhibition of the MAPK pathway (Montero et al., 2019; Nangia et al., 2018). Interestingly, co-treatment with the selective MCL1 inhibitor S63845 shortened D_O but also more than doubled MEKi-induced D_R, from less than 2% h^{-1} to over 4% h^{-1} in $A549^N$ cells (Figures 4F and 4G). This effect was specific to MEKis, as MCL1 inhibition did not alter D_R in response to the proteasome inhibitor bortezomib (Figures 4F and 4G). S63845 also accelerated the rate of MEKi-induced FK in Calu-6^N NSCLC cells and U-2 OS^N osteosarcoma cells, albeit to different degrees (Figures S4J-S4L). Consistent with the small-molecule inhibitor data, CRISPR/Cas9-mediated *MCL1* disruption enhanced the rate of MEKi-induced FK (Figures S4M and S4N, and see below). Thus, MCL1 appeared to serve as an important negative regulator of the rate of MEKi-induced FK. Of note, MCL1 inhibition or genetic inactivation alone was not lethal, and in concert with our cycloheximide data (Figures S4A and S4D), we infer that the induction of a pro-death protein such as BIM is necessary for the induction of cell death even when MCL1 is completely inactivated.

Given the above results, we examined how MCL1 expression varied between individual cells, as determined using protein immunofluorescence, in response to MEKi treatment. As a comparison, we also examined the expression of BCL-xL. Consistent with our bulk analysis, Pim treatment (5 μM; 48 h) reduced single-cell BCL-xL protein levels (Mann-Whitney test, $p < 0.0001$) (Figure 4H). BCL-xL expression was also more homogeneous between cells following Pim treatment, as inferred from the coefficient of variation in protein expression (Figure 4H). By contrast, total levels of MCL1 increased following Pim treatment, and variation in MCL1 expression between cells remained high (Figure 4H). Indeed, when examined in response to MEKi treatment over time, MCL1 levels became increasingly variable between surviving cells over time, as assessed either by coefficients of variation or the range of absolute MCL1 expression between remaining live cells (Figure 4I). Since this analysis detects only live cells, we cannot determine whether surviving cells have higher levels of MCL1 prior to drug exposure or whether they are able to accumulate MCL1 more quickly in response to drug exposure, although the latter possibility seems most likely given that less variability in MCL1 levels between cells is apparent at earlier than later time points (see also below). Regardless, based on these results, we hypothesized that higher levels of MCL1 over time would slow FK, perhaps by allowing for greater sequestration of proapoptotic BH3-only proteins. Consistent with this model, enforced MCL1 overexpression significantly reduced the rate of FK (i.e., D_R) in response to MEKis (Figures 4J-4L). These results suggest that variable MCL1 expression contributes to the rate of FK in response to MAPK pathway inhibitors.

The Regulation of FK Is Lethal Stimulus Specific

Whether the molecular mechanisms governing FK vary between lethal stimuli, or are shared, is poorly understood. Our evidence suggested that the mechanisms governing FK in response to MEKis were unlikely to be shared with other lethal molecules. Further support for this model was obtained from the analysis of a series of 15 (sub-) clonal cell lines isolated from our starting population of $A549^N$ cells, each exposed to Pim (5 μM), Tram (0.5 μM), bortezomib (Btz) (50 nM), or erastin2 (Era2) (2 μM), and examined in parallel using time-lapse imaging (Figure 5A). Substantial variability was observed been these clonal

populations in the rate and total amount (i.e., LF_{max}) of MEKi-induced FK within the period of observation, while more consistent responses between all clones were observed in response to both Btz and Era2 (Figure 5B). This directly demonstrates that the molecular mechanisms governing FK in response to MEKis are distinct from those contributing to FK in response to other lethal stimuli.

These clonal cell lines provided an opportunity to examine whether differences in MEKi-induced FK related to differences in the expression of MCL1. Based on our existing data (Figures 4H-4L), we hypothesized that high levels of MCL1 expression would correlate with lower sensitivity to MEKi-induced FK. To test this hypothesis, we picked clones that exhibited relatively low (#6 and #15) or high (#10 and #16) sensitivity to MEKi-induced FK and examined protein expression. Both low- and high-sensitivity clones exhibited similar basal phosphorylated ERK1/2 and BCL-xL expression, and similar loss of both species following MEKi treatment (Figure 5C). By contrast, low-sensitivity clones accumulated substantially higher levels of MCL1 and BIM following MEKi treatment compared to high-sensitivity clones (Figure 5C). Thus, high levels of MCL1 accumulation correlates with slower MEKi-induced FK, possibly due to a greater capacity to “buffer” the accumulation of pro-death proteins like BIM.

The pathway linking MAPK pathway inhibition to increased MCL1 levels was unclear. In our RNA-seq analysis, we observed increased expression of several JUN-family immediate-early genes, consistent with activation of the JNK pathway (Figure S5). This was intriguing as in other systems JNK1/2 can modulate apoptosis by phosphorylating and stabilizing MCL1 (Hirata et al., 2013; Kodama et al., 2009). We confirmed activation of the JNK pathway in response to MEKi treatment by qRT-PCR and western blotting for JUN family members in parental $A549^N$ cells (Figures 5D and 5E). Moreover, we observed that inhibition of JNK function using the small-molecule inhibitor JNKi VIII (Miura et al., 2018) inhibited JUN expression and phosphorylation, and reduced MCL1 accumulation in response to MEKi treatment, without affecting BCL-xL or BIM levels (Figure 5E). Thus, inhibition of the MAPK pathway can activate the stress-responsive JNK pathway, which may allow for stabilization of the antiapoptotic MCL1 protein and inhibition of FK, although further investigation is required to understand how JNK signaling regulates FK via MCL1 at the molecular level.

Compound Interactions Alter MEKi-Induced Fractional Killing over Time

The most effective cancer treatments involve combinations of lethal agents (Palmer et al., 2019). It is therefore of interest to understand how drug interactions may alter the kinetics of FK over time. We showed, above, that it was possible to detect chemical interactions that enhance the rate of FK (e.g., MEKis + MCL1 inhibition; Figure 4F). We figured that our ability to monitor FK in many populations in parallel would enable us to search more systematically for modulators of FK kinetics. As proof-of-principle, we examined how Pim-induced FK was modulated in $A549^N$ cells by 261 structurally and functionally distinct compounds targeting a variety of intracellular pathways (Figures 6A and S6A). The ability of all 261 compounds to modulate Pim-induced FK was computed using an analytic framework based on the Bliss model of drug interactions (Conlon et al., 2019). Strikingly,

multiple ATP-competitive and allosteric mechanistic target of rapamycin (mTOR) inhibitors potently enhanced Pim-induced FK, decreasing D_O, increasing D_R by as much as 5-fold, and increasing LF_{max} substantially within the period of observation, leading to near-complete cell eradication (Figures 6B and S6B). The top enhancers of cell death were not lethal alone, suggesting that the observed synergy was not due to a nonspecific interaction between toxic compounds (Figure S6B). We found that MEKi-induced FK was suppressed by diverse compounds, including the corticosteroid dexamethasone and the cyclin-dependent kinase inhibitor flavopiridol (Figures S6A and S6C). These compounds may limit MEKi-induced FK by altering the expression of proapoptotic or antiapoptotic genes, or by some other mechanism, and were not investigated further here. Cell cycle state and proliferative arrest can influence MCL1 levels (Harley et al., 2010). However, compounds that potently arrested cell proliferation alone were found among both the enhancers and suppressors of MEKi-induced FK, suggesting that the observed modulatory effects were not tied in any simple way to cell cycle state (Figure S6D). These results indicate that it is possible to pinpoint drug interactions in a high-throughput manner that specifically alter the rate of FK.

Our observation that mTOR inhibitors accelerated MEKi-induced FK was interesting in light of evidence that mTOR signaling promotes *MCL1* mRNA expression and post-translational MCL1 stability (Koo et al., 2015; Mills et al., 2008). Based on these findings, we hypothesized that mTOR inhibition accelerated MEKi-induced FK by reducing MCL1 expression. We confirmed that two structurally and mechanistically distinct mTOR inhibitors, the ATP competitive inhibitor AZD8055 and the allosteric inhibitor rapamycin, both accelerated the rate of MEKi-induced FK specifically in $A549^N$ cells, with no sensitization observed toward bortezomib (Figure 6C). However, mTOR inhibitors did not reduce basal MCL1 expression or prevent Pim treatment from increasing MCL1 protein levels in $A549^N$ cells (Figure 6D). We confirmed that mTOR inhibitors blocked the phosphorylation of the canonical downstream mTOR targets RPS6 and/or 4EBP1 and did not alter the effect of Pim on BIM upregulation or BCL-xL downregulation, suggesting that inhibition of the MAPK pathway was unaffected (Figure 6D).

These results suggested that mTOR signaling might enhance the rate of FK independent of effects on MCL1. To investigate further, we generated two clonal *MCL1* gene disrupted cell lines, one (LOF1) that appeared to be a severe loss of function, and one (LOF2) that appeared to be a complete knockout, based on MCL1 protein expression and sensitivity to the MCL1 inhibitor S63845 (Figures 6E and 6F). Consistent with results obtained using the polyclonal CRISPR method (Figure S4K and S4L), the rate of MEKi-induced FK was substantially accelerated in cells where MCL1 was disrupted (Figure 6E). Notably, mTOR inhibition enhanced the rate of MEKi-induced FK equivalently in the presence or absence of MCL1. This suggests that mTOR inhibition may increase the rate of MEKi-induced FK upstream of MCL1 inhibition. These results demonstrate that it is possible to systematically search for and isolate compound-compound interactions that alter the kinetics of FK.

DISCUSSION

Anticancer drugs typically kill only a fraction of cells within a population, at least at a given time. Using high-throughput population imaging, the STACK method, lethal fraction

scoring, and associated analytical strategies, we have been able to highly parallelize the analysis of drug-induced FK. By enabling us to examine FK under diverse settings, we have made two observations that bear on the interpretation of FK *in vitro*. First, for many lethal compounds tested here, raising the concentration by as little as a factor of 4 could promote a transition from low FK to near-complete FK, where up to 99% of all cells within the population were eventually eradicated. This suggests that FK can be threshold-dependent, need not correlate in any linear manner with drug dose, and cannot always be explained by the prescence of large numbers of drug-tolerant persister cells. Second, the apparent FK within a population can vary as a function of time. Thus, even when using saturating drug concentrations that would likely eliminate differences between cells in drug uptake and target engagement, substantial differences were apparent between individual cells in the initiation of cell death. This may be important for the analysis of FK *in vitro*, and for thinking about how best to achieve high levels of FK *in vivo* while minimizing toxicity, perhaps by modulating drug dosing schedules.

As a case study to search for molecular modulators of FK, we focused on inhibitors of the MAPK pathway. Here, a simple explanation for differences in the total amount or rate of FK could be variable inhibition of the MAPK pathway itself between cells, either due to incomplete target engagement or activation of compensatory feedback pathways (Keyse, 2008). In $A549^N$ cells, however, we observed that MEKis were only toxic when the MAPK pathway was completely inhibited. This implied that factors outside the MAPK pathway itself were likely key regulators of FK. In particular, we find that MCL1 plays an important role in the regulation of FK in response to MAPK pathway inhibition. MCL1 expression may be inherently highly variable between cells due to the short half-life of *MCL1* mRNA and the instability of the protein (Senichkin et al., 2020). Our pharmacological, imaging, and overexpression studies suggest that differences in the rate of FK are linked in part to variation in MCL1 protein expression between cells within the population, with the ability to accumulate higher levels of MCL1 in a given cell associated with later onset of cell death (Figure 6G). We speculate that higher levels of MCL1 could lengthen the time it takes for the entire MCL1 pool within a given cell to be fully overcome by gradual upregulation of pro-death BH3 proteins like BIM.

The observed differences in sensitivity to MEKis observed in the isolated clonal cell lines further suggests that the parental population likely contains numerous distinct subpopulations of cells, varying in their capacity to accumulate MCL1 and thereby evade death. We infer that inactivation of MCL1 helps homogenize the responses of individual cells to MAPK pathway inhibition, resulting in an apparent acceleration of FK over time. That said, MCL1 inactivation does not render cells uniformly sensitive to death at the exact same time, either in these clonal cell lines or the parental population (i.e., D_R remains under 10% h^{-1}). This indicates that other processes impact fractional killing in the models examined here, including potentially the expression of other pro-death proteins such as NOXA (Montero et al., 2019).

Looking ahead, at least three questions require further elucidation. First, what are the MCL1-independent mechanisms that govern FK in response to MAPK pathway inhibition in A549 and other cells? Evidence from our compound interaction analysis suggests that one

mechanism involves mTOR, perhaps through regulation of a proapoptotic protein like BAD (Harada et al., 2001). Second, how generalizable across cell lines is the role of MCL1 in regulating FK in response to MAPK pathway inhibition? We find that MCL1 inhibition has a more important role in some cell types (i.e., A549, U-2 OS) than others (i.e., Calu-6). The basis for this difference is presently unclear. Third, how generalizable is the role of MCL1 in regulating FK in response to other lethal stimuli, apart from MAPK pathway inhibition? Here, we show that MCL1 inhibition or accumulation has little impact on apoptotic cell death induced by proteasome inhibition or ferroptotic cell death induced by a system x_c^- inhibitor, erastin2. Thus, even within a single cell type, MCL1 is not a universal regulator of FK in response to all lethal stimuli. Moreover, proteins and mechanisms that regulate FK or FK-like phenomena in other contexts, including p53 induction, ROS accumulation, and cell proliferation, do not appear to modulate FK in response to MAPK pathway inhibition in our models. Collectively, our results suggest that FK emerges from the interaction of numerous molecular mechanisms that in many cases will be lethal stimulus and context specific. This concept implies that personalized medicine strategies will likely be needed to overcome drug tolerance in cancer patients.

STAR★METHODS

RESOURCE AVAILABILITY

Lead Contact—Further information and requests for resources and reagents should be directed to and will be fulfilled by the Lead Contact, Scott Dixon (sjdixon@stanford.edu).

Materials Availability—Plasmids generated in this study have been deposited to AddGene and are also available from the authors. Cell lines are available from the authors.

Data and Code Availability—RNA sequencing data generated as part of this study is available from the Gene Expression Omnibus (accession number: GSE140172). STACK analysis for the 261 compound interaction screen is available through the Mendeley Data Repository at https://doi.org/10.17632/9bccjb75wp.1.

EXPERIMENTAL MODEL AND SUBJECT DETAILS

The following cell lines were obtained from ATCC (Manassas, VA): A549 (CCL-185, sex: male), Calu-6 (HTB-56, sex: female), NCI-H1299 (CRL-5803, sex: male), NCI-H2291 (CRL-5939, sex: male), T98G (CRL-1690, sex: male), U-2 OS (HTB-96, sex: female) and HEK293T cells (CRL-3216, sex: female). Cell lines stably-expressing nuclear-localized mKate2 (denoted by the superscript ‘N’) were generated by infection with lentivirus (Cat# 4625, Essen BioScience, Ann Arbor, MI) followed by puromycin (10 μg/mL, Cat# A11138-03, Life Technologies, Carlsbad, CA) selection for three days. For kinase translocation reporter (KTR) and polyclonal CRISPR cell lines described below, mKate2-expressing cell lines were generated with a bleomycin-selectable lentiviral construct (Cat# 4627, Essen BioScience) to allow subsequent infection and selection with puromycin-selectable markers. After infection with bleomycin-selectable lentivirus, cell lines were sorted to isolate mKate2-positive cells using a FACSAria II Fluorescence Activated Cell Sorter (BD Biosciences, San Jose, CA) at the Stanford Shared FACS Facility.

Cell lines were cultured in an appropriate base media supplemented with 10% fetal bovine serum (Cat# 26140-079, Thermo Fisher Scientific) and 1% penicillin/streptomycin (Cat# 105070-063, Life Technologies). Base media used was DMEM (Cat# MT-10-013-CV, Thermo Fisher Scientific) for A549, Calu-6, NCI-H1299 (H1299), T98G, and HEK293T, RPMI (Cat# SH30027FS, Thermo Fisher Scientific) for NCI-H2291, and McCoy's 5A (Cat# MT-10-050-CV, Thermo Fisher Scientific) for U-2 OS. Cell lines were cultured in incubators at 37°C and 5% CO_2. For passaging, cells were rinsed with HBSS (Cat# 14025-134, Life Technologies), dissociated with 0.25% trypsin-EDTA (Cat# SH3004201, Thermo Fisher Scientific), quenched with the corresponding complete media, and counted using a Cellometer Auto T4 Bright Field Cell Counter (Nexcelom, Lawrence, MA). Upon counting, cells were subsequently seeded for experiments as described below.

METHOD DETAILS

Chemicals and reagents—Camptothecin (Cat# S1288), vinblastine (Cat# S1248), pimasertib (Cat# S1457), trametinib (Cat# S2673), ABT-737 (Cat# S1002), A-1155463 (Cat# S7800), and nutlin-3 (Cat# S1061) were purchased from Selleck Chemicals (Houston, TX). Bortezomib (Cat# NC0587961), etoposide (Cat# ICN19391825), MG-132 (Cat# 17-485), and Q-VD-OPh (Cat# OPH00101M) were purchased from Thermo Fisher Scientific. N-acetylcysteine (Cat# A8199), thapsigargin (Cat# T9033), tunicamycin (Cat# T7765), paclitaxel (Cat# T7191), JNK Inhibitor VIII (Cat# 420135), 2-deoxyglucose (Cat# D8375), oligomycin (Cat# O4876), and cycloheximide (Cat# C7698) were obtained from Sigma-Aldrich (St. Louis, MO). S63845 (Cat#21131) was obtained from Cayman Chemical (Ann Arbor, MI). Staurosporine (Cat# A8192) was obtained from ApexBio (Houston, TX). Erastin was the kind gift of Brent Stockwell (Columbia University). Erastin2 (compound 35MEW28 in Dixon et al., [2014]) and ML162 (CAS: 1035072-16-2) were synthesized by Acme Bioscience (Palo Alto, CA). Chemical screening was conducted as described below; the library of 261 bioactive compounds was obtained from Selleck Chemicals (Cat# L2000).

Lentivirus generation and infection—For generation of lentivirus, HEK293T cells were seeded at 300,000 cells per well in six well plates (Cat# 07-200-83, Thermo Fisher Scientific) one day before transfection. Plasmids for lentiviral transduction were transfected into HEK293T cells along with lentiviral packaging plasmids pCMV-VSV-G, pMDLg/pRRE, and pRSV-Rev (obtained from Dr. Michael Bassik, available via Addgene as Cat# 8454,12251, and 12253). Transfection was conducted using PolyJet Transfection Reagent (Cat# SL100688, SignaGen Laboratories, Rockville, MD) according to manufacturer instructions, using a plasmid mix of 0.25 μg pCMV-VSV-G, 0.25 μg pMDLg/pRRE, 0.25 μg pRSV-Rev, and 0.75 μg of the appropriate transfer plasmid. Lentivirus-containing supernatant from the transfected cells was harvested 48 and 72 hours after transfection and filtered through a 0.45 μm Millex filter (Cat# SLHV033RS, EMD Millipore, Burlington, MA) using a 10 mL syringe (Cat# 14-817-30, Thermo Fisher Scientific). Filtered lentivirus was stored at −80°C or used immediately. For infection, cell lines were seeded a day before infection in 12 well plates (Cat# 07-200-82, Thermo Fisher Scientific) to be approximately 50% confluent on the day of infection. On the day of infection, supernatant was removed from the cells and replaced with 500 μL of lentivirus-containing media and 500 μL of polybrene (Cat# H9268-5G, Sigma-Aldrich, St. Louis, MO) diluted to a final concentration

of 16 μg/mL in the appropriate complete media. Selection with the appropriate antibiotic was begun after two days.

Generation of CRISPR/Cas9 knockouts—Two methods were used to generate CRISPR/Cas9 knockout cell lines, one yielding polyclonal knockout lines and the other clonal knockout cell lines. Polyclonal knockout cell lines were generated by lentiviral infection of cell lines with the lentiCas9-Blast plasmid and an MCL1 sgRNA-expressing plasmid. lentiCas9-Blast was a gift from Feng Zhang (Addgene plasmid #52962; RRID: Addgene_52962). sgRNA expressing plasmids were produced by cloning sgRNA oligonucleotides with the appropriate adaptor sequences (see Table S2) into plasmid pMCB306 after digesting the plasmid with restriction enzymes BstXI and Bpu1120I (Cat# FD1024, FD0094, Thermo Fisher Scientific). pMCB306 was a gift from Michael Bassik (Addgene plasmid #89360; RRID: Addgene_89360). After infection and antibiotic selection (10 μg/mL blasticidin or puromycin for three days), knockout cell lines were validated by western blot.

Clonal CRISPR/Cas9 knockout cell lines were generated as described previously (Cao et al., 2019). Briefly, sgRNA expressing plasmids were produced by cloning sgRNA oligonucleotides with the appropriate adaptor sequences (see Table S2) into plasmid spCas9-2A-EGFP (PX458). spCas9-2A-EGFP (PX458) was a gift from Feng Zhang (Addgene plasmid #48138; RRID: Addgene_48138). Knockout cell lines were generated from mKate2-expressing A549 cells generated with a bleomycin-selectable lentiviral construct. Cells were seeded and transfected with the sgMCL1-expressing plasmid in a 6 well plate using Lipofectamine LTX transfection reagent (Cat# 15338030, Thermo Fisher Scientific) according to manufacturer's instructions. 2 days after transfection, single cells were isolated and sorted into a 96 well plate using an Influx Special Order fluorescence activated cell sorter (BD Biosciences, San Jose, CA) at the Stanford Shared FACS Facility. Cells were sorted into DMEM media supplemented with 30% fetal bovine serum (Cat# 26140-079, Thermo Fisher Scientific) and 1% penicillin/streptomycin (Cat# 105070-063, Life Technologies). Clones were monitored and expanded to larger formats over the following 4 weeks, then validated for MCL1 knockout by western blot.

Isolation of clonal cell populations—Single-cell clones were isolated and expanded from mKate2-expressing A549 cells. Low passage cells were trypsinized and brought to the Stanford Shared FACS facility for single cell sorting as described for CRISPR clone sorting above. Two sets of twelve clones were passaged into new 96 well plates on days 23 and 25 after sorting. Each set of clones was treated with lethal drugs the day after seeding and monitored by Incucyte for 144 hours. Clones with insufficient cell number or heterogeneous expression of mKate2 were excluded from analysis. When seeded for drug treatment, clones were also expanded to obtain cell lysates for protein expression analysis. Cells were harvested and lysed for Western Blotting as described below, and protein expression was compared across clones.

Cell seeding and compound treatment—Experiments measuring death after treatment with MEK inhibitors (or other lethal compounds), either alone or in combination with modulators (e.g., CHX, Q-VD-OPh, or Bcl-2 family inhibitors), were conducted as follows.

Cells were seeded one day prior to compound addition in tissue culture treated clear-bottom 96- or 384-well plates (Fisher Scientific Cat# 07-200-588, 07-201-013). Appropriate cell seeding density was determined for each cell line to ensure seeding dense enough for cells to proliferate normally and sparse enough to minimize death due to overcrowding before the end of the experiment. On the day of treatment, compounds were diluted to final doses in the appropriate cell culture media noted above. Seeding media was removed from the plate and replaced with compound-containing media. For experiments to be analyzed by STACK, 20 nM SYTOX Green dye (Life Technologies, Cat# S7020) was included in the treatment media, and drug treated plates of cells were imaged every 4 h using an IncuCyte. Images were analyzed automatically as described below. For drug cycling experiments, cells were seeded in 384-well plates. On the day of compound removal, a multichannel pipette was used to remove the compound-containing media and wash once with normal media before adding normal media to the wells for the compound-untreated period.

Gene overexpression—To generate doxycycline-inducible cell lines, cells were infected with lentivirus carrying the pLenti CMV rtTA3 Blast (w756-1) plasmid and selected with blasticidin (Cat# A1113902, Thermo Fisher Scientific). Genes of interest were cloned into the pLenti CMVTRE3G eGFP Neo (w821-1) plasmid using a Gibson Assembly Master Mix kit (Cat# E2611S, New England Biolabs, Ipswich, MA). pLenti CMV rtTA3 Blast (w756-1) and pLenti CMVTRE3G eGFP Neo (w821-1) were gifts from Eric Campeau (Addgene plasmids #26429 and #27569; RRIDs: Addgene_26429 and Addgene_27569). *BCL2L1* (BCL-xL) and both wild-type and G156E mutant *BCL2L11* (BIM) open reading frames for Gibson Assembly were obtained as custom synthesized gBlocks from Integrated DNA Technologies (Coralville, IA). Lentivirus was generated as described above and rtTA-expressing cell lines were infected and subsequently selected with 10 μg/mL Geneticin (Thermo Fisher Scientific, Cat# 11811-031); complete selection with Geneticin required three passages in antibiotic. An uninfected control population was treated with Geneticin and passaged in parallel to ensure complete selection.

Overexpression of *MCL1* was carried out using the pLenti CMV Puro DEST backbone. pLenti CMV Puro DEST (w118-1) was a gift from Eric Campeau & Paul Kaufman (Addgene plasmid# 17452; RRID: Addgene_17452). The open reading frame for *MCL1* was obtained as a gift from Dr. Aaron Gitler as a pDONR plasmid from the human ORFeome library. The MCL1 ORF was cloned into the pLenti CMV vector using a Gateway LR Clonase II kit (Cat# 11791-020, Thermo Fisher Scientfic, Waltham, MA).The resulting plasmid is missing a stop codon; site-directed mutagenesis was carried out using the Q5 Site-Directed Mutagenesis Kit (New England Biolabs, Cat# E0554S) to introduce a stop codon. Lentivirus was generated as described above, generating virus with both the CMV-MCL1 plasmid and the control backbone plasmid that did not undergo Gateway recombination. Cell lines were infected with the harvested virus, and infected cells were selected with 5 μg/mL puromycin for three days.

Cell death kinetic analysis—Scalable time-lapse analysis of cell death kinetics (STACK) experiments were performed as described previously (Forcina et al., 2017). Image analysis was conducted using IncuCyteZoom software (Essen BioScience). Image analysis

parameters were optimized for each cell line; parameters are listed in Table S1. Lethal fraction scoring, LED curve fitting and parameter extraction were carried out as described previously (Forcina et al., 2017). Red and green object counts were used to the compute the lethal fraction at each time point and then analyzed further using Prism 7 software (GraphPad, San Diego, CA). For experiments presented in Figure 3 onward, overlap (red and green dual-positive) objects were also quantified and subtracted from red object counts before the lethal fraction calculation was performed (although these objects still weakly express mKate2, the uptake of SYTOX green indicates that they are most accurately classified as dead cells). Lethal fraction curves were fit using the ‘‘plateau followed by one-phase association” function to obtain an LED fit. D_O (corresponding to X0 in Prism) and D_R (corresponding to K in Prism) values were extracted from the successful curve fits. D_R values in % h^{-1} were obtained by multiplying the K value by 100. For parameter analysis in Figure 2, only lethal compound conditions yielding average lethal fraction scores > 0.5 across all three independent experiments were examined. The death span was for lethal compounds was computed by subtracting the time point where the lethal fraction first exceeded 0.75 from the time point when the lethal fraction first exceed 0.25.

Kinase translocation reporter analysis—The kinase translocation reporter (KTR) cell line was generated by lentiviral transduction of the pLentiCMV Puro DEST ERKKTRClover plasmid (gift of Dr. Markus Covert, obtained via Addgene, Cat# 59150). Infected cells were selected with 10 μg/mL puromycin for 3 days. For drug treatment experiments, periodic IncuCyte imaging started the day after seeding and continued for 24 hours before drug addition to establish an untreated baseline. No more than 30 min before the 24 h time point, seeding media was removed from the cells and drug-containing media was added to the plate. To analyze the collected images, Zoom analysis parameters were modified as listed in Table S1. KTR reporter was detected in the green channel in lieu of SYTOX Green in these experiments. mKate2 signal marked cell nuclei, and cells in which the KTR reporter translocated to the nucleus produced a dual-positive overlap signal that was quantified in the software.

Cell metabolism and ROS analysis—For analysis of glycolytic and oxidative metabolism upon drug treatment, $A549^N$ cells were seeded in normal media in Seahorse xFP plates (Cat# 103022-100, Agilent Technologies, Santa Clara, CA) 24 h prior to conducting the assay. Sensor cartridges were also hydrated on the preceding day. On the day of the assay, cells were washed with complete Seahorse XF media (Cat# 103334-100, Agilent Technologies) supplemented to final concentrations of 25 mM glucose, 1 mM pyruvate, and 4 mM glutamine and adjusted to pH 7.4. After washing twice and replacing media with complete XF media, plates were imaged by IncuCyte to obtain cell counts for normalization and the plate was incubated in a non-CO2 incubator for one hour to de-gas. 10X solutions of drugs for injection (oligomycin, 2-DG, and ethanol vehicle control) were loaded into the sensor cartridge, and the cell plate and sensor cartridge were inserted into a Seahorse xFP Analyzer (Agilent Technologies) to obtain extracellular acidification rate (ECAR) and oxygen consumption rate (OCR) metrics. ECAR and OCR values were measured automatically approximately every 6 minutes; after four baseline measurements, drugs were

injected from the cartridge and metabolic parameters were measured continuously over the remainder of the experiment.

For FACS analysis of ROS levels, cells were trypsinized and resuspended in HBSS containing 20 uM H_2DCFDA (Thermo Fisher Scientific, Cat# D-399). Cells were incubated in a 37°C, 5% CO_2 incubator for 30 min to stain, then spun down at 1000 rpm for 5 min. H_2DCFDA containing supernatant was aspirated, and the pellet of stained cells was resuspended in HBSS and strained through a 35 μm mesh filter into a test tube (Corning, Cat# 352235) for sorting. Cells were sorted on a FACSAria II Fluorescence Activated Cell Sorter (BD Biosciences, San Jose, CA) at the Stanford Shared FACS Facility. The top and bottom 5% of cells based on H_2DCFDA were sorted into DMEM, counted, and seeded in 384 well plates prepared with diluted drugs before the sort. IncuCyte imaging began the following day and images were acquired once every 24 h.

Western blotting—Cells for western blot analysis were treated in 6 well plates (Thermo Fisher Scientific, Cat# 07-200-83) or 10 cm dishes (USA Scientific, Ocala, FL, Cat# CC7682-3394). At the time of harvest, treatment media was removed, and cells were washed with ice cold HBSS and detached with cell lifters (Fisher Scientific, Cat# 07-200-364). Detached cells in HBSS were spun down at 1000 rpm for 5 min, then supernatant was removed, and the remaining pellets were frozen overnight at −80°C. NP-40 buffer (1% NP-40 detergent, 50 mM Tris-Cl pH 8.0,150 mM NaCl) was used for lysis. NP-40 buffer was supplemented with protease/phosphatase inhibitor cocktail (Cell Signaling Technology, Danvers, MA, Cat# 5872S) and used to lyse frozen pellets. Lysis proceeded for 45 min on ice, then samples were sonicated for 10 pulses of 1 s each at 50% amplitude with a Fisherbrand Sonic Dismembrator (Fisher Scientific, Cat# FB120110). Lysates were centrifuged for 15 min at 12,700 rpm to remove debris, then protein concentration was measured by BCA assay kit (Thermo Fisher Scientific, Cat# 23252).

Lysates were combined with Bolt sample buffer and reducing agent (Thermo Fisher Scientific, Cat# B0007, B0009) and heated for 10 min at 70°C. Prepared samples were loaded onto Bolt 4%–12% gradient gels (Thermo Fisher Scientific, Cat# BG04120BOX) and run for 1 hour 45 min at 100 mV. Protein from the finished gel was transferred to a nitrocellulose membrane using an iBlot 2 Transfer stack (Invitrogen, Cat# IB23002). Membranes were washed in Odyssey Blocking buffer (LI-COR Biosciences, Lincoln, NE) at room temperature for 1 hour, then incubated in primary antibody mixture overnight at 4°C. Primary antibody incubation was followed by three seperate seven min washes in Tris-Buffered Saline + 0.1% Tween (TBS-T), then a 45 min room temperature incubation in secondary antibody mix. Membranes were washed three more times in TBS-T before imaging on an Odyssey CLx imaging system (LiCOr Biosciences). In cases where antibodies against both the phopho and total protein were used, both forms of the protein were blotted sequentially on the same membrane. The phosphorylated version of the protein was blotted first; after imaging, the membrane was stripped with a 20 min wash in NewBlot Nitro Stripping Buffer followed by three TBS-T washes. Membranes were then reprobed by the same protocol using an antibody mix targeting the total protein.

RNA analysis—For RNA-Seq and RT-qPCR experiments, RNA was harvested from cells grown in six-well plates. For A549 cells, 150,000 cells were seeded into each well. The next day, cells were treated with either vehicle control (DMSO), a cytostatic, non-lethal concentration of pimasertib (0.5 μM) or a cytotoxic, lethal concentration of pimasertib (5 μM). Calu-6 cells were seeded at 300,000 cells per well and the next day treated with DMSO or Pim (5 μM). For RNA-Seq experiments, treatments were carried out for 96 h prior to cell harvest. In vehicle-treated conditions, cells were split 1:8 after 24 hours of treatment to prevent overgrowth. Note: for lethal conditions (i.e., 5 μM Pim), treatment for 96 h resulted in ~50% cell death at the time of cell harvest. At the time of harvest, treatment media was removed, and cells were washed with ice cold HBSS (to remove debris) and detached with cell lifters. Detached cells were pelleted (1000 rpm x 5 min), the HBSS supernatant was removed, and the cell pellets frozen at −80°C overnight. The next day, cells were lysed and RNA extracted using a Qiashredder Kit and RNeasy Plus Mini Kit (QIAGEN, Cat# 796554, 74134). For RNA-seq analysis, purity, concentration, and integrity of RNA were assessed by NanoDrop Spectrophotomer (Thermo Fisher Scientific) and by Eukaryote Total RNA Nano chip analysis on a Bioanalyzer (Agilent) at the Stanford Protein and Nucleic Acid Facility. By Bioanalyzer, the RNA Integrity Number for each sample met a threshold of at least 6.8, and NanoDrop 260/280 and 260/230 ratios met a threshold of at least 1.95. After quality control, samples were shipped on dry ice to Novogene (Sacramento, CA) for library generation and 20M read PE150 sequencing on an Illumina HiSeq 4000 platform. Bioinformatic analysis was performed by Novogene. Reads with adaptor contamination, >10% uncertain nucleotides, or >50% nucleotides with base quality <20 were filtered out, and the remaining clean reads (at least 98% of reads in all conditions) were aligned to the reference genome using Tophat v2.0.12. At least 91% of clean reads were successfully mapped in all conditions. Pearson correlations between biological replicates yielded R^2 values above 0.98 in all conditions. Gene expression analysis was performed using DESeq 1.10.1; we isolated all gene sequences that were significantly altered (adjusted $P\ value < 0.05$). For RT-qPCR experiments, primers were designed using available information (Kolomeichuk et al., 2008; Spandidos et al., 2010) and performed under conditions as described previously (Tarangelo et al., 2018).

Propidium iodide cell cycle profiling—Cell cycle profiling of A549 cells was performed after treatment with drugs in a 6 well plate as described above. At the end of drug treatment, cells were washed with HBSS, trypsinized, and quenched, keeping the drug treatment media and HBSS wash for each condition to avoid loss of any loosely adherent dividing cells. Cells from each condition were spun down (500 x g, 5 min), resuspended in HBSS for one wash, then spun down again. Each pellet was resuspended in 400 μL HBSS, then 800 μL ice cold 100% ethanol was added for fixation. Cells were fixed at4°Cforat least 1 hour and up to 3 weeks. When ready to be stained, fixed cells were equilibrated to room temperature, then pelleted and resuspended in HBSS containing 50 μg/mL propidium iodide (Thermo Fisher Scientific, Cat# P3566) and 500 U/mL RNase A (Thermo Fisher Scientific, Cat# EN0531). Staining was carried out for 30 minutes at 37°C, then cells were spun down, resuspended in HBSS for one wash, then spun down again. For analysis, cells were resuspended in HBSS and run on a FACSCalibur flow cytometer (BD Biosciences). Histograms of signal from the FITC channel were analyzed in FlowJo 10.6.1, using the Cell

Cycle platform to estimate percentages of cells in each cell cycle phase based on propidium iodide signal.

Immunofluorescence imaging—A549 cells were seeded in 12-well plates for immunofluorescence and treated with drugs as described above. When seeding for immunofluorescence, 12 mm round glass #1.5 coverslips (Electron Microscopy Sciences, Hatfield, PA, Cat# 72230-01) coated with poly-D-lysine (Sigma-Aldrich, Cat# P0899) were placed in each well of the 12 well plate, allowing cells to adhere to the coverslips before treatment. Once drug treatment was complete, drug-containing media was removed and cells were washed once with PBS. PBS was removed and replaced with ice cold methanol (Fisher Scientific, Cat# A935-4) to fix cells; fixation was carried out at −20°C for at least one hour and up to 72 h. To stain fixed cells, methanol was removed and replaced with PBS for one wash, then coverslips were blocked in PBS containing 3% bovine serum albumin (Gemini Bio-Products, West Sacramento, CA, Cat# 700-100P) 0.1% Triton X-100 (Sigma-Aldrich, Cat# X-100), and 0.02% sodium azide (Sigma-Aldrich, Cat# S2002) (PBS-BT). Blocking was carried out for 1 hour at room temperature or overnight at 4°C. After blocking, coverslips were transferred to a light-blocking, parafilm-coated humid chamber for staining. All staining solutions were made in PBS-BT, and all subsequent steps were carried out at room temperature. Primary antibody mixes were applied to coverslips for one hour, followed by 3 washes with PBS-BT. Secondary antibodies (Goat anti-rabbit Alexa Fluor 568 and Goat anti-mouse Alexa Fluor 488, Life Technologies, Cat# A11036 and A11029) were applied subsequently for one hour, followed by an additional 3 PBS-BT washes. Finally, nuclear staining was carried out by applying 100 ng/mL DAPI (Thermo Fisher Scientific, Cat# D1306) for 15 min, followed by 5 washes with PBS-BT. Coverslips were mounted on microscope slides (Thermo Fisher Scientific, Cat# 12-544-1) using Prolong Gold Antifade mounting media (Thermo Fisher Scientific, Cat# P10144). Coverslips were imaged using a Lionheart FX Automated Microscope (BioTek, Winooski, VT), taking images using the GFP, Texas Red, and DAPI filter cubes at each imaged position. For each condition, 20 images were collected and all cells in each image were analyzed using CellProfiler 3.0.0 (McQuin et al., 2018) (Broad Institute, Cambridge, MA). A modified CellProfiler analysis pipeline was created based on the example “Fruit fly cells” pipeline available at https://cellprofiler.org/examples/, excluding all cells whose cytoplasm was not contained fully within the image field. Calculated per-cell mean fluorescence intensity values were extracted for the GFP and Texas Red channels from each image and plotted in Prism.

Chemical library screening—To screen for small molecule modulators of Pim-induced death, $A549^N$ cells were seeded in two parallel 384-well plates. A library of 261 bioactive compounds (Selleck Chemicals, Cat# L2000) was diluted in SYTOX Green-containing DMEM from 2 mM to 50 μM in a dilution plate using a Versette liquid handler (Thermo Fisher Scientific). The day after seeding, the liquid handler was used to pipette SYTOX Green-containing media with either Pim or DMSO vehicle control into the assay plates containing $A549^N$ cells. The compound library from the dilution plate was subsequently added to each assay plate, diluting the library 10X. The resulting assay plates contained $A549^N$ cells treated with either 5 μM Pim or DMSO, plus the library compounds at a 5 μM dose. The plates were subsequently analyzed by STACK, imaging on an IncuCyte (Essen

BioScience) every 4 h for 120 h total and processed and analyzed as described above. Three independent replicates of the library screen were conducted, with subsequent analysis performed using the mean of the lethal fraction (LF) for the three replicates at each time point.

Compound interactions were scored as follows. Normalized area under the curve (nAUC) metrics were calculated and compared using a Bliss model of drug independence. nAUC was calculated by generating an AUC value from the LF curve and dividing this value by the maximum possible AUC: an LF value of 1 at every time point measured. A mean nAUC value for Pim was calculated from DMSO control wells in the Pim-treated plates from all three replicates. Using the nAUC values for Pim (P) and each library compound (L) in the DMSO-treated plate, an expected nAUC (E) was calculated for each combination of Pim plus the library compound based on the Bliss model: $E = P + L - (P * L)$. The deviation of the observed nAUC from this expected nAUC represented the enhancement or protection of Pim-induced death by the library compound. Three library compounds (sunitinib malate, mitoxantrone and PHA-665752) were found to be auto-fluorescent under our assay conditions and removed from the analysis, leaving 258 compounds in the final analysis.

QUANTIFICATION AND STATISTICAL ANALYSIS

Lethal fraction scores were computed using Microsoft Excel 14.6.0 (Microsoft Corporation, Redmond, WA). LED curve fitting was performed using Prism 8 (GraphPad Software, La Jolla, CA). Flow cytometry data were analyzed using FlowJo 10.6.1 (FlowJo LLC, Ashland, OR). Immunofluorescence images were quantified using CellProfiler 3.0.0 (Broad Institute, Cambridge, MA). Graphing and statistical analyses were performed using Prism 8. Figures were assembled using Adobe Illustrator (Adobe Systems, San Jose, CA). Statistical details of experiments and statistical tests used can be found in the main text, figure legends, and STAR Methods. For all experiments, *n* indicates the number of times an experiment was repeated on separate days.

Supplementary Material

Refer to Web version on PubMed Central for supplementary material.

ACKNOWLEDGMENTS

We thank L. Magtanong for comments, A. Gitler for plasmids, and B. Stockwell for erastin. S.J.D. is supported by the NIH (1R01GM122923) and a Damon Runyon-Rachleff Innovation Award.

REFERENCES

Berenbaum MC (1972). In vivo determination of the fractional kill of human tumor cells by chemotherapeutic agents. Cancer Chemother. Rep 56, 563–571. [PubMed: 4652587]

Bigger J (1944). Treatment of staphylococcal infections with penicillin by intermittent sterilisation. Lancet 244, 497–500.

Cao JY, Poddar A, Magtanong L, Lumb JH, Mileur TR, Reid MA, Dovey CM, Wang J, Locasale JW, Stone E, et al. (2019). A Genomewide Haploid Genetic Screen Identifies Regulators of Glutathione Abundance and Ferroptosis Sensitivity. Cell Rep. 26, 1544–1556.e8. [PubMed: 30726737]

Conlon M, Poltorack C, Forcina GC, Wells A, Mallais M, Kahanu A, Magtanong L, Pratt DA, and Dixon SJ (2019). A compendium of kinetic cell death modulatory profiles identifies ferroptosis regulators. bioRxiv. 10.1101/826925.

Cragg MS, Jansen ES, Cook M, Harris C, Strasser A, and Scott CL (2008). Treatment of B-RAF mutant human tumor cells with a MEK inhibitor requires Bim and is enhanced by a BH3 mimetic. J. Clin. Invest 118, 3651–3659. [PubMed: 18949058]

Dixon SJ, Patel DN, Welsch M, Skouta R, Lee ED, Hayano M, Thomas AG, Gleason CE, Tatonetti NP, Slusher BS, and Stockwell BR (2014). Pharmacological inhibition of cystine-glutamate exchange induces endoplasmic reticulum stress and ferroptosis. eLife 3, e02523. [PubMed: 24844246]

Fallahi-Sichani M, Honarnejad S, Heiser LM, Gray JW, and Sorger PK (2013). Metrics other than potency reveal systematic variation in responses to cancer drugs. Nat. Chem. Biol 9, 708–714. [PubMed: 24013279]

Forcina GC, Conlon M, Wells A, Cao JY, and Dixon SJ (2017). Systematic quantification of population cell death kinetics in mammalian cells. Cell Syst. 4, 600–610.e6. [PubMed: 28601558]

Harada H, Andersen JS, Mann M, Terada N, and Korsmeyer SJ (2001). p70S6 kinase signals cell survival as well as growth, inactivating the proapoptotic molecule BAD. Proc. Natl. Acad. Sci. USA 98, 9666–9670. [PubMed: 11493700]

Harley ME, Allan LA, Sanderson HS, and Clarke PR (2010). Phosphorylation of Mcl-1 by CDK1-cyclin B1 initiates its Cdc20-dependent destruction during mitotic arrest. EMBO J. 29, 2407–2420. [PubMed: 20526282]

Hata AN, Yeo A, Faber AC, Lifshits E, Chen Z, Cheng KA, Walton Z, Sarosiek KA, Letai A, Heist RS, et al. (2014). Failure to induce apoptosis via BCL-2 family proteins underlies lack of efficacy of combined MEK and PI3K inhibitors for KRAS-mutant lung cancers. Cancer Res. 74, 3146–3156. [PubMed: 24675361]

Hirata Y, Sugie A, Matsuda A, Matsuda S, and Koyasu S (2013). TAK1-JNK axis mediates survival signal through Mcl1 stabilization in activated T cells. J. Immunol 190, 4621–4626. [PubMed: 23547112]

Inde Z, and Dixon SJ (2018). The impact of non-genetic heterogeneity on cancer cell death. Crit. Rev. Biochem. Mol. Biol 53, 99–114. [PubMed: 29250983]

Keyse SM (2008). Dual-specificity MAP kinase phosphatases (MKPs) and cancer. Cancer Metastasis Rev. 27, 253–261. [PubMed: 18330678]

Kim C, and Giaccone G (2018). MEK inhibitors underdevelopment for treatment of non-small-cell lung cancer. Expert Opin. Investig. Drugs 27, 17–30.

Kodama Y, Taura K, Miura K, Schnabl B, Osawa Y, and Brenner DA (2009). Antiapoptotic effect of c-Jun N-terminal kinase-1 through Mcl-1 stabilization in TNF-induced hepatocyte apoptosis. Gastroenterology 136, 1423–1434. [PubMed: 19249395]

Kolomeichuk SN, Terrano DT, Lyle CS, Sabapathy K, and Chambers TC (2008). Distinct signaling pathways of microtubule inhibitors—vinblastine and Taxol induce JNK-dependent cell death but through AP-1-dependent and AP-1-independent mechanisms, respectively. FEBS J. 275, 1889–1899. [PubMed: 18341588]

Koo J, Yue P, Deng X, Khuri FR, and Sun S-Y (2015). mTOR complex 2 stabilizes Mcl-1 protein by suppressing its glycogen synthase kinase3-dependent and SCF-FBXW7-mediated degradation. Mol. Cell. Biol 35, 2344–2355. [PubMed: 25918246]

Lu H, Iuliano JN, and Tonge PJ (2018). Structure-kinetic relationships that control the residence time of drug-target complexes: insights from molecular structure and dynamics. Curr. Opin. Chem. Biol 44, 101–109. [PubMed: 29986213]

Marani M, Tenev T, Hancock D, Downward J, and Lemoine NR (2002). Identification of novel isoforms of the BH3 domain protein Bim which directly activate Bax to trigger apoptosis. Mol. Cell. Biol 22, 3577–3589. [PubMed: 11997495]

Mateus A, Gordon LJ, Wayne GJ, Almqvist H, Axelsson H, Seashore-Ludlow B, Treyer A, Matsson P, Lundbäck T, West A, et al. (2017). Prediction of intracellular exposure bridges the gap between target- and cell-based drug discovery. Proc. Natl. Acad. Sci. USA 114, E6231–E6239. [PubMed: 28701380]

McQuin C, Goodman A, Chernyshev V, Kamentsky L, Cimini BA, Karhohs KW, Doan M, Ding L, Rafelski SM, Thirstrup D, et al. (2018). Cell-Profiler 3.0: next-generation image processing for biology. PLoS Biol. 16, e2005970. [PubMed: 29969450]

Meng J, Fang B, Liao Y, Chresta CM, Smith PD, and Roth JA (2010). Apoptosis induction by MEK inhibition in human lung cancer cells is mediated by Bim. PLoS ONE 5, e13026. [PubMed: 20885957]

Mills JR, Hippo Y, Robert F, Chen SMH, Malina A, Lin C-J, Trojahn U, Wendel H-G, Charest A, Bronson RT, et al. (2008). mTORC1 promotes survival through translational control of Mcl-1. Proc. Natl. Acad. Sci. USA 105, 10853–10858. [PubMed: 18664580]

Miura H, Kondo Y, Matsuda M, and Aoki K (2018). Cell-to-cell heterogeneity in p38-mediated cross-inhibition of JNK causes stochastic cell death. Cell Rep. 24, 2658–2668. [PubMed: 30184500]

Montero J, Gstalder C, Kim DJ, Sadowicz D, Miles W, Manos M, Cidado JR, Paul Secrist J, Tron AE, Flaherty K, et al. (2019). Destabilization of NOXA mRNA as a common resistance mechanism to targeted therapies. Nat. Commun 10, 5157. [PubMed: 31727958]

Nangia V, Siddiqui FM, Caenepeel S, Timonina D, Bilton SJ, Phan N, Gomez-Caraballo M, Archibald HL, Li C, Fraser C, et al. (2018). Exploiting MCL1 dependency with combination MEK + MCL1 inhibitors leads to induction of apoptosis and tumor regression in KRAS-mutant non-small cell lung cancer. Cancer Discov. 8, 1598–1613. [PubMed: 30254092]

Paek AL, Liu JC, Loewer A, Forrester WC, and Lahav G (2016). Cell-to-cell variation in p53 dynamics leads to fractional killing. Cell 165, 631–642. [PubMed: 27062928]

Palmer AC, Chidley C, and Sorger PK (2019).A curative combination cancer therapy achieves high fractional cell killing through low cross-resistance and drug additivity. eLife 8, e50036. [PubMed: 31742555]

Raha D, Wilson TR, Peng J, Peterson D, Yue P, Evangelista M, Wilson C, Merchant M, and Settleman J (2014). The cancer stem cell marker aldehyde dehydrogenase is required to maintain a drug-tolerant tumor cell subpopulation. Cancer Res. 74, 3579–3590. [PubMed: 24812274]

Regot S, Hughey JJ, Bajar BT, Carrasco S, and Covert MW (2014). High-sensitivity measurements of multiple kinase activities in live single cells. Cell 157, 1724–1734. [PubMed: 24949979]

Roux J, Hafner M, Bandara S, Sims JJ, Hudson H, Chai D, and Sorger PK (2015). Fractional killing arises from cell-to-cell variability in overcoming a caspase activity threshold. Mol. Syst. Biol 11, 803. [PubMed: 25953765]

Santos LC, Vogel R, Chipuk JE, Birtwistle MR, Stolovitzky G, and Meyer P (2019). Mitochondrial origins of fractional control in regulated cell death. Nat. Commun 10, 1313. [PubMed: 30899020]

Senichkin VV, Streletskaia AY, Gorbunova AS, Zhivotovsky B, and Kopeina GS (2020). Saga of Mcl-1: regulation from transcription to degradation. Cell Death Differ. 27, 405–419. [PubMed: 31907390]

Shaffer SM, Dunagin MC, Torborg SR, Torre EA, Emert B, Krepler C, Beqiri M, Sproesser K, Brafford PA, Xiao M, et al. (2017). Rare cell variability and drug-induced reprogramming as a mode of cancer drug resistance. Nature 546, 431–435. [PubMed: 28607484]

Sharma SV, Lee DY, Li B, Quinlan MP, Takahashi F, Maheswaran S, McDermott U, Azizian N, Zou L, Fischbach MA, et al. (2010). A chromatin-mediated reversible drug-tolerant state in cancer cell subpopulations. Cell 141, 69–80. [PubMed: 20371346]

Spandidos A, Wang X, Wang H, and Seed B (2010). PrimerBank: a resource of human and mouse PCR primer pairs for gene expression detection and quantification. Nucleic Acids Res. 38, D792–D799. [PubMed: 19906719]

Spencer SL, Gaudet S, Albeck JG, Burke JM, and Sorger PK (2009). Non-genetic origins of cell-to-cell variability in TRAIL-induced apoptosis. Nature 459, 428–432. [PubMed: 19363473]

Tarangelo A, Magtanong L, Bieging-Rolett KT, Li Y, Ye J, Attardi LD, and Dixon SJ (2018). p53 suppresses metabolic stress-induced ferroptosis in cancer cells. Cell Rep. 22, 569–575. [PubMed: 29346757]

Wolpaw AJ, Shimada K, Skouta R, Welsch ME, Akavia UD, Pe'er D, Shaik F, Bulinski JC, and Stockwell BR (2011). Modulatory profiling identifies mechanisms of small molecule-induced cell death. Proc. Natl. Acad. Sci. USA 108, E771–E780. [PubMed: 21896738]

Highlights

- Fractional killing can be quantified for hundreds of populations in parallel
- Fractional killing is inherently time dependent
- Different lethal stimuli trigger fractional killing with unique kinetics
- MCL1 can regulate fractional killing kinetics in response to MEK1/2 inhibitors

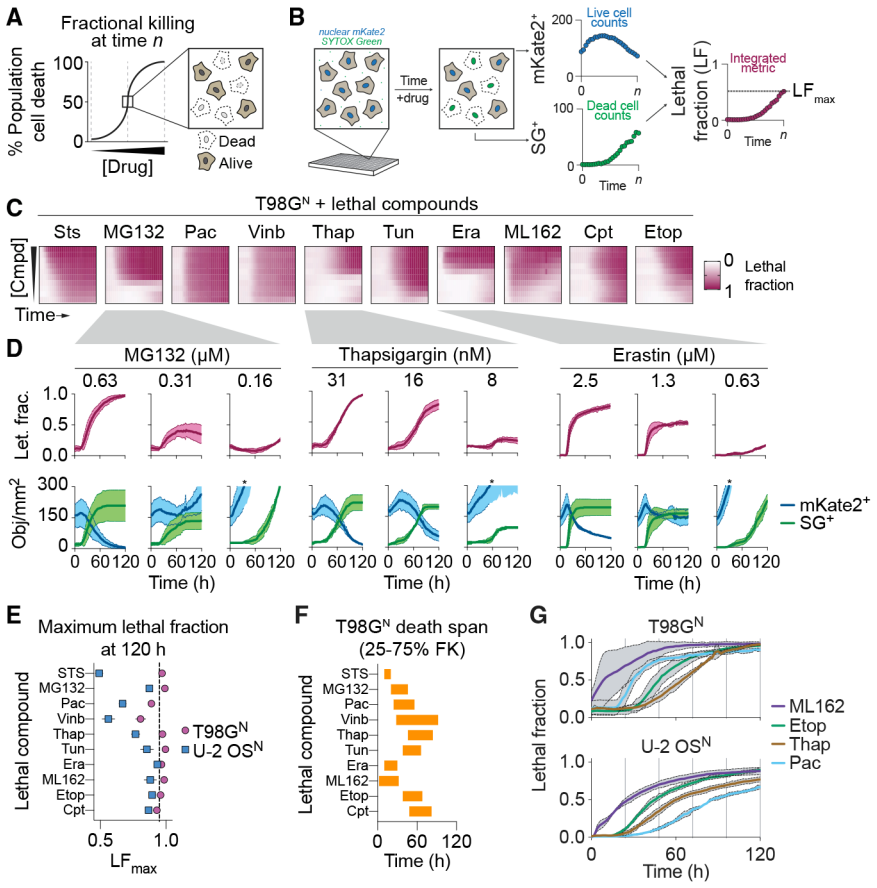

Figure 1. Systematic Investigation of Fractional Killing

(A) Illustration of dose-dependent fractional killing at a given time point.

(B) Overview of cell death analysis using the STACK approach, yielding lethal fraction scores over time and a maximum lethal fraction score (LF_{max}).

(C) Lethal fraction scores summarized over time (x axis) and by compound concentration (y axis) for 10 compounds in $T98G^N$ cells. Cmpd, compound; Sts, staurosporine; Pac, paclitaxel; Vinb, vinblastine; Thap, thapsigargin; Tun, tunicamycin; Era, erastin; Cpt, camptothecin; Etop, etoposide.

(D) Lethal fraction (Let. frac.) scores and corresponding live ($mKate2^+$) and dead (SG^+) cell counts, represented as objects/mm^2 imaged area (Obj./mm^2), extracted from select conditions in (C). The asterisks (*) indicates conditions where population live cell counts exceed the boundary of the y axis, due to high rates of proliferation, and are not plotted.

(E) Maximum lethal fraction scores for U-2 OS^N and $T98G^N$ cells exposed to the highest tested compound concentrations.

(F) Death span for the tested compounds in $T98G^N$ cells. The yellow bars encompass the time span between when LF first exceeded 0.25 and when LF first exceeded 0.75, for the highest tested dose of each compound.

(G) Mean lethal fractions at select time points from the data presented in (C) and Figure S1A. ML162 (8 μM), Etop (200 μM), Thap (0.25 μM), and Pac (0.5 μM). Data are from three independent experiments and represent the mean (C and F) or mean ± SD (D, E, and G).

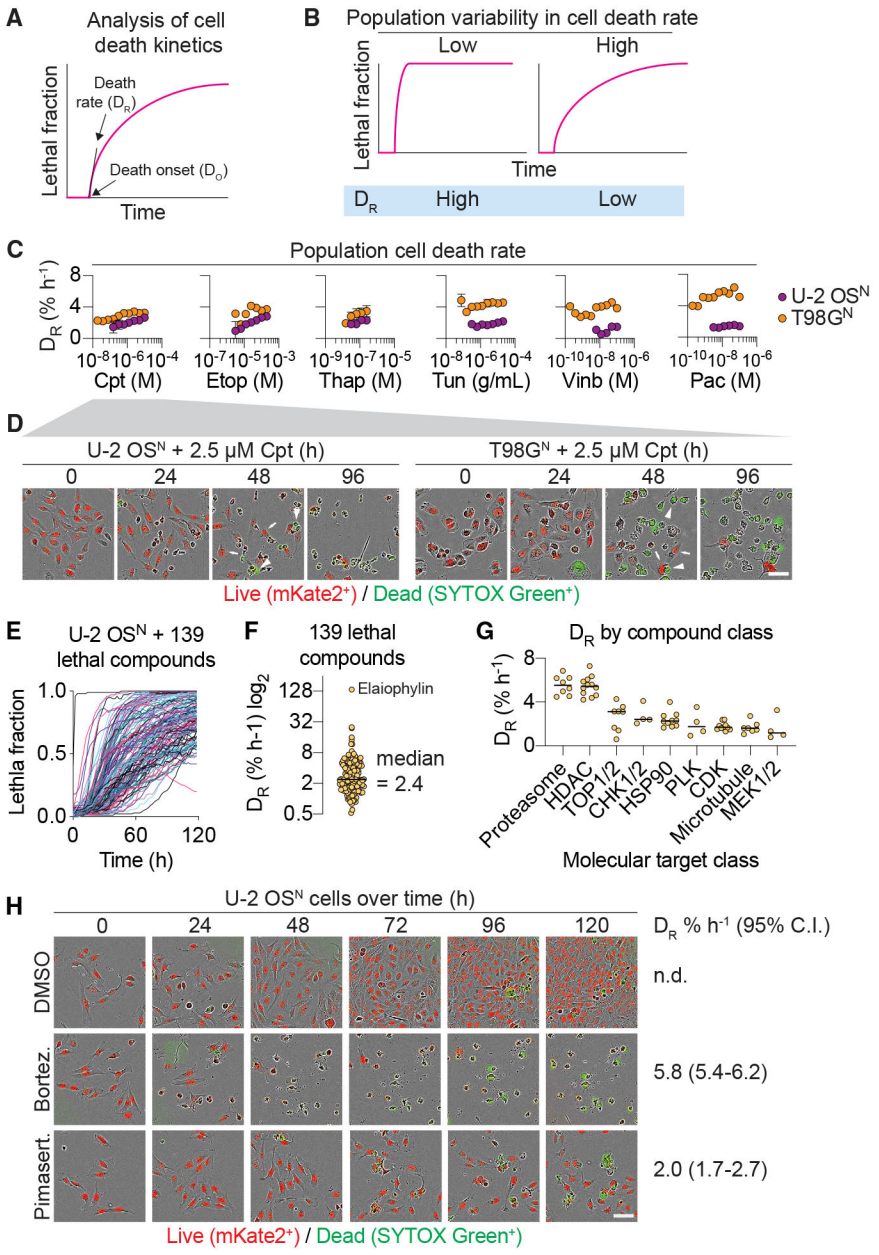

Figure 2. Quantification of Time-Dependent Fractional Killing

(A) Overview of cell death kinetic analysis using lag exponential death (LED) curves (pink) fit to lethal fraction scores over time. The parameter values D_O and D_R reflect the timing of cell death onset and the maximum rate of cell death within the population, respectively (Forcina et al., 2017).

(B) Treatments that trigger cell death with low between-cell variability will have high D_R values and vice versa.

(C) Extracted D_R parameter values for a subset of the lethal compounds shown in Figures 1D and S1G. Kinetic parameter values were only computed for compound concentrations where the lethal fraction at 120 h exceeded 0.5. Results are mean ± SD from three independent experiments.

(D) Representative population images over time for camptothecin (Cpt)-treated cells. Variability in cell death within the population is apparent at the 48-h time point. The arrows indicate example live cells, and the arrowheads indicate example dead cells. Scale bar, 75 μm.

(E) Traces of lethal fraction scores over time for 139 mechanistically diverse lethal compounds, each tested at 5 μM, in $T98G^N$ cells.

(F) Extracted D_R values for 139 lethal compounds from (E) where it was possible to compute this parameter value. Elaiophylin is an outlier compound that likely directly permeabilizes the plasma membrane causing instantaneous death.

(G) D_R values for compounds in (F) broken down by compound class.

(H) Representative population images for select conditions from (G) to illustrate variability in cell death initiation throughout the population. Bortez., bortezomib; Pimasert., pimasertib. Scale bar, 75 μm.

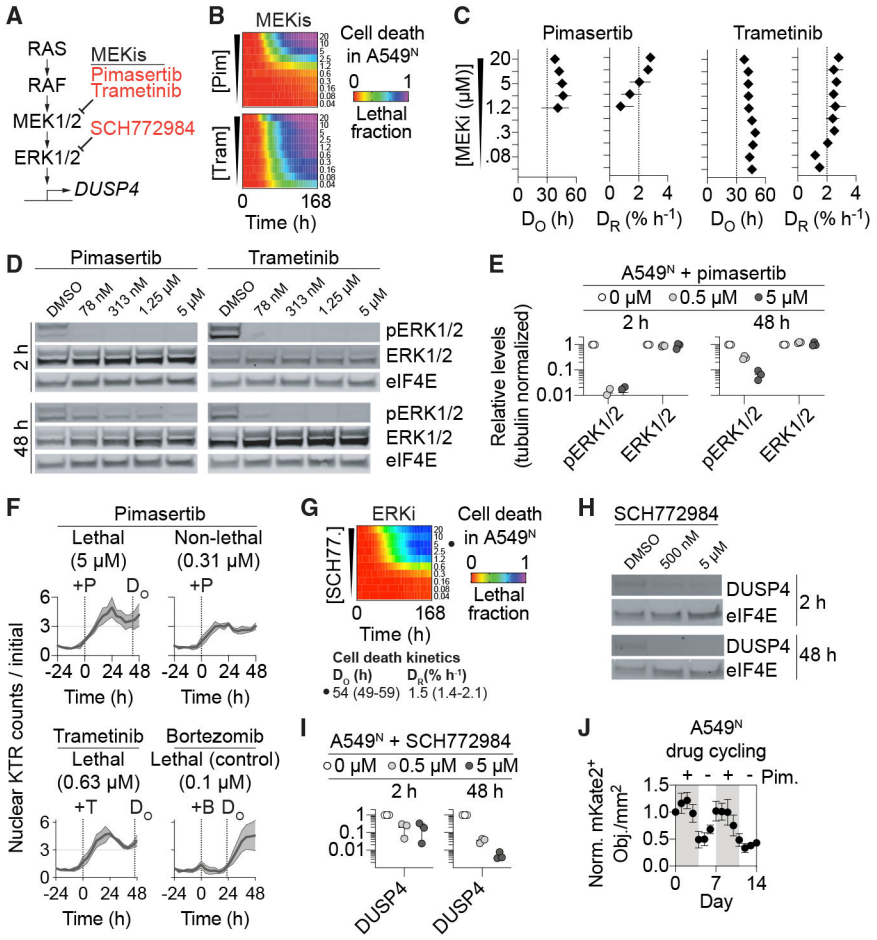

Figure 3. MEKis Trigger Cell Death with High Between-Cell Variability

(A) Outline of key RAS/MAPK pathway components highlighting inhibitors (red) of MEK1/2 (i.e., MEKis) and ERK1/2.

(B) Cell death in A549^{N} cells summarized over time and MEKi concentration.

(C) Cell death kinetic parameters for the data in (B) summarized over compound concentration. Note: parameters can only be computed with confidence for compound concentrations with lethal fraction greater than ~0.2.

(D) Western blot for phosphorylated and total ERK1/2 in A549^{N} cells.

(E) Quantification of phospho-ERK1/2 and total ERK1/2 at different concentrations of pimasertib at two time points.

(F) Data for ERK kinase translocation reporter (KTR) in A549^{N} cells in response to MEKi treatment over time. Compound addition is indicated by the plus (+) sign. ERK KTR response to an unrelated lethal compound, bortezomib, is shown as a control. Death onset for lethal conditions (from B and C for MEKis and not shown for Btz) is shown by a dashed line (D_O).

(G) Cell death in A549^{N} cells summarized over time and concentration for the ERK inhibitor (ERKi) SCH772984. Cell death kinetic parameter values are shown for cells treated with 5 μM SCH772984 (SCH77.).

(H) Expression of the MAPK pathway target DUSP4 in response to SCH772984.

(I) Quantification of conditions shown in (H), for three separate blots.
(J) Normalized live cell (mKate2^{+} objects) counts within the same population of cells over two cycles of pimasertib (Pim, 5 μM, gray shaded area) addition with an intervening period of regrowth in the absence of drug (white area). All data are from at least three independent experiments and represent the mean (B and G), mean ± 95% confidence interval (C), or mean ± SD (E, F, I, and J).

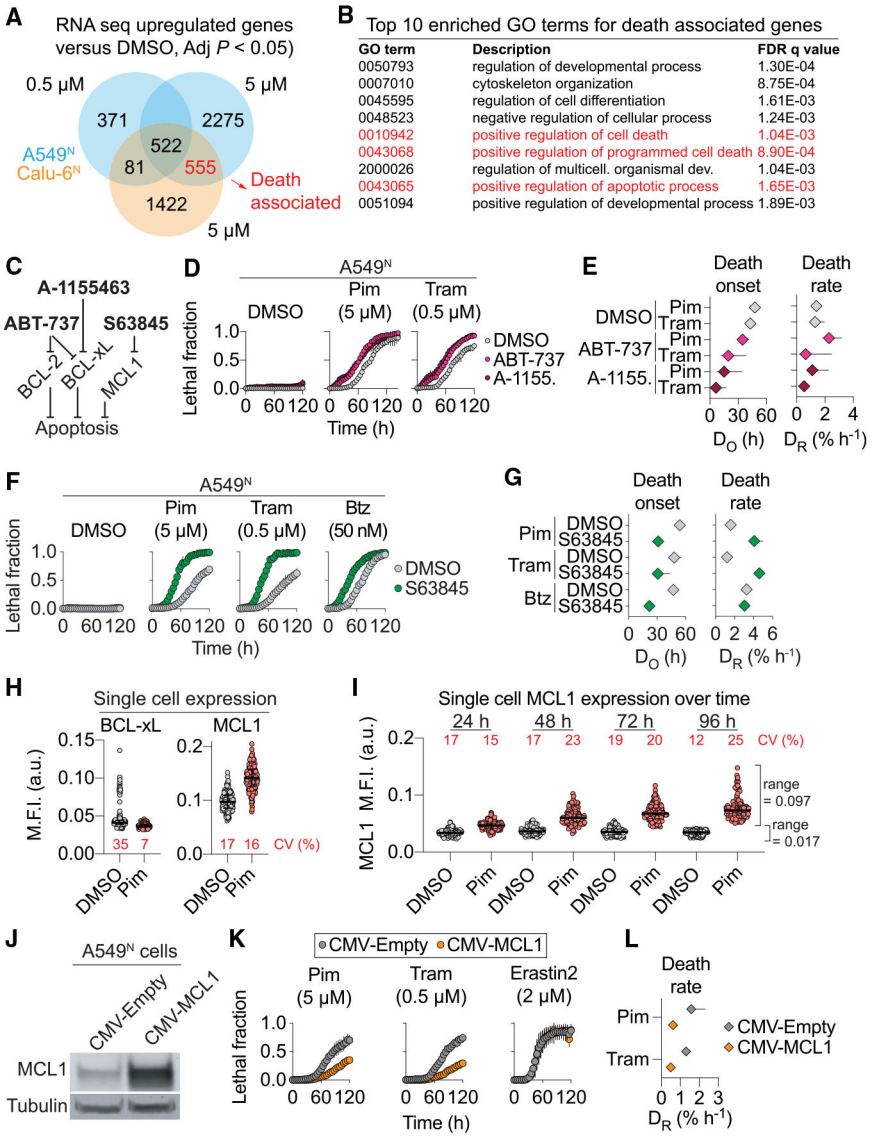

Figure 4. Variable Mcl-1 Expression Correlates with MEKi-Induced FK

(A) Summary of upregulated genes identified by RNA-sequencing analysis of cells treated with pimasertib at cytotoxic (5 μM, A549 and Calu-6) and cytostatic but noncytotoxic (0.5 μM in A549) doses. RNA was obtained for analysis from two independent experiments, and FPKM (fragments per kilobase of exon per million reads) values for each gene were averaged prior to further analysis.

(B) Gene ontology (GO) analysis for the 555 significantly altered death-associated genes.

(C) Inhibitors (bold text) block the function of BCL-2-family proteins to induce apoptosis.

(D) Cell death over time in A549^N cells co-treated with MEKis and the BCL-xL inhibitors ABT-737 or A-1155463 (A-1155.). BCL-xL inhibitors were used at 5 μM.

(E) Cell death kinetic parameters for treatments in (D).

(F) Cell death over time in A549^N cells co-treated with MEKis or bortezomib (Btz) and the MCL1 inhibitor S63845 (5 μM).

(G) Cell death kinetic parameters for treatments in (F).

(H) Mean single-cell fluorescence intensity (M.F.I.) for MCL1 and BCL-xL in individual $A549^N$ cells determined by immunofluorescence at 48 h ± Pim (5 μM). Coefficient of variation (CV) is indicated. a.u., arbitrary units.

(I) MCL1 M.F.I. over time in $A549^N$ cells treated as indicated. Coefficient of variation (CV) is shown for all conditions, and ranges (min-max) are shown for the 96-h sample. For (H) and (I), at least 115 individual cells are quantified per condition from multiple independent microscopic fields, and median and interquartile ranges are indicated.

(J) Expression of MCL1 in $A549^N$ cells transduced with CMV-Empty and CMV-MCL1 lentivirus.

(K) Cell death over time ± MCL1 overexpression, as in (J).

(L) D_R values computed from lethal fraction curves in K for MEKis. Results are from three independent experiments and represent the mean ± SD (D, F, and K) or the mean ± 95% C.I. (E, G, and L).

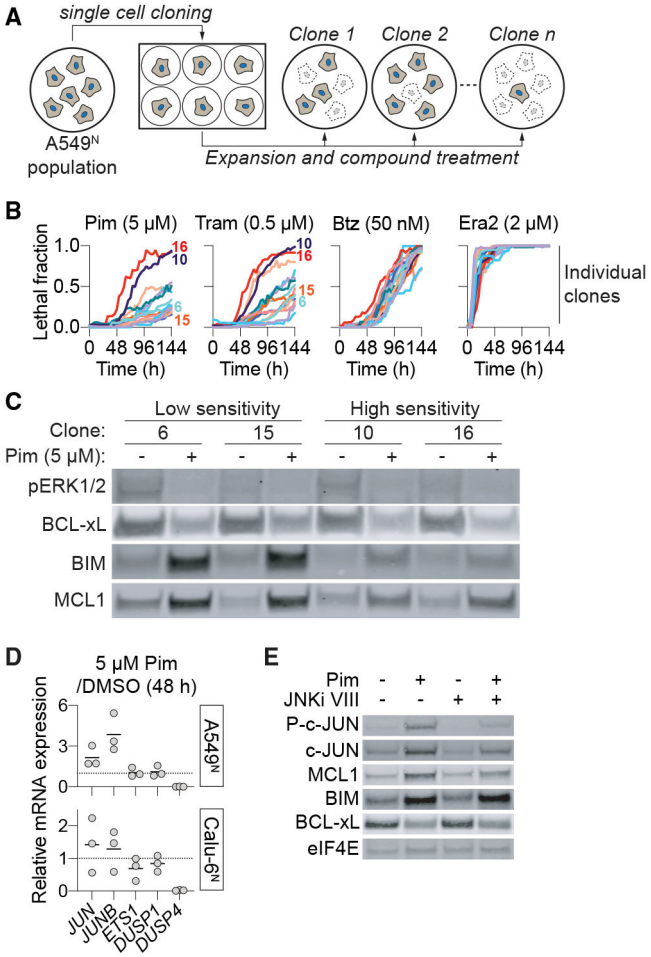

Figure 5. Variable MCL1 Expression Correlates with Death Sensitivity

(A) Overview of the strategy used to isolate clonal populations of A549^{N} cells.

(B) FK over time for individual clonal populations examined in parallel. Each independent clone was derived from a single cell, expanded, and tested a single time. Key clones analyzed at the protein level in (C) are numbered. Pim, pimasertib; Tram, trametinib; Btz, bortezomib; Era2, erastin2.

(C) Expression of key apoptotic proteins in low- and high-sensitivity clones.

(D) qRT-PCR analysis of selected immediate-early genes. Individual data points represent individual experiments, and mean values are indicated by the horizontal bar. The dotted line indicates a fold-change of 1.

(E) Western blot of A549^{N} cells. Pim and JNK inhibitor (JNKi) VIII were both used at 5 μM.

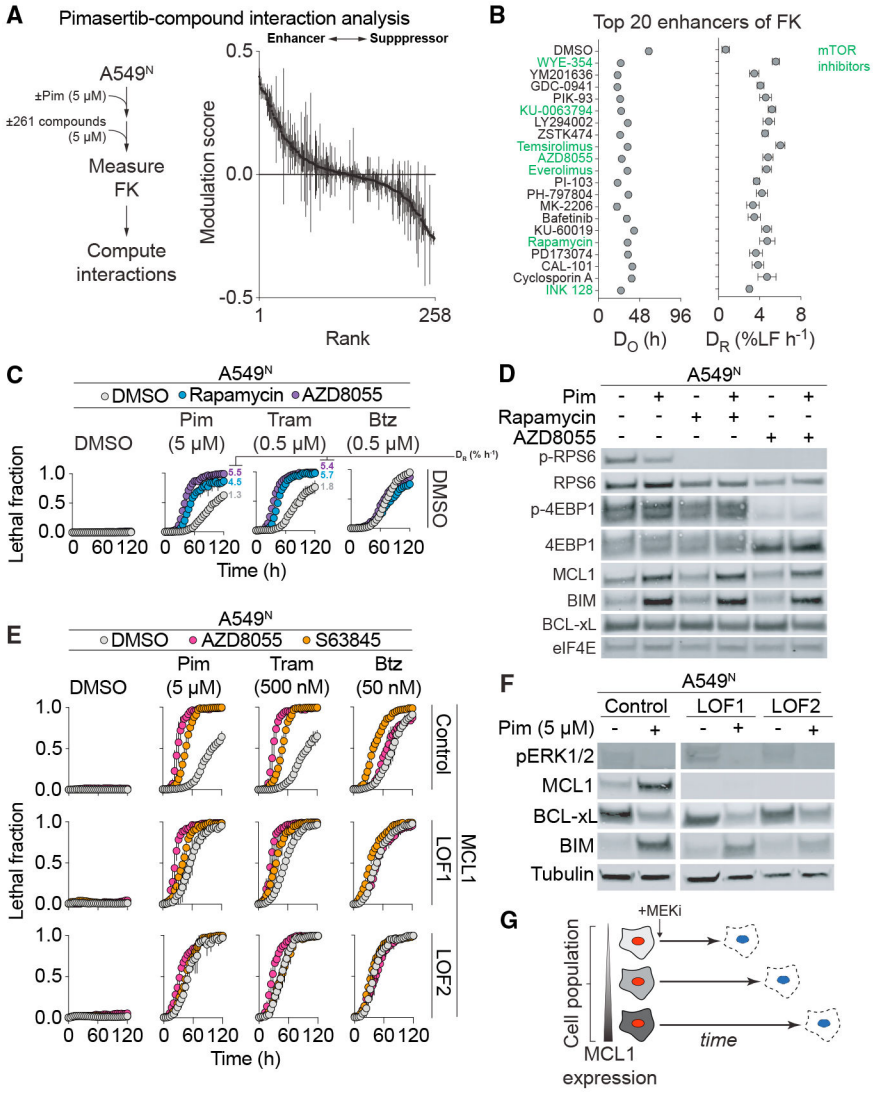

Figure 6. High-Throughput Analysis of Compound Interactions Impacting Fractional Killing

(A) A compound interaction screen in pimasertib (Pim)-treated A549^N cells. Cells were co-treated ± 5 μM Pim plus a library of 261 bioactive compounds and controls. Data on the y axis (modulation score) represent deviations between the observed normalized area under the curve (nAUC) value from the expected nAUC value for each library compound in combination with Pim, as calculated using the Bliss model of drug independence (see STAR Methods). The screen was performed three separate times, and the results represent mean ± SD. Positive values indicate FK that was enhanced beyond expectation, and negative values indicate FK that was suppressed below expectation.

(B) Kinetics of cell death computed for the top 20 enhancers of Pim-induced cell death. mTOR inhibitors are indicated in green.

(C) Cell death over time for the indicated combinations. Rapamycin (50 nM) and AZD8055 (500 nM) were not lethal alone, and in the leftmost panel these data are obscured underneath the DMSO curve. Mean D_R values were computed from lethal fraction curves and are indicated. Tram, trametinib; Btz, bortezomib.

(D) Analysis of protein expression by western blotting ± Pim (5 μM), rapamycin (50 nM), or AZD8055 (500 nM) at 48 h.
(E) Cell death over time in control and two independent MCL1 loss-of-function clones (LOF1/2).
(F) Protein expression in control and MCL1 LOF1/2 cell lines. Compound treatment was for 48 h.
(G) Model expressing how variability in MCL1 expression links to variable membrane permeabilization (i.e., cell death) over time. Data are from three independent experiments and represent mean ± 95% CI (B) or mean ± SD (C and E).

KEY RESOURCES TABLE

REAGENT or RESOURCE	SOURCE	IDENTIFIER
Antibodies		
Anti-Tubulin alpha (mouse)	Fisher Scientific	Cat# MS581P1; RRID: AB_144075
Anti-eIF4E (mouse)	Santa Cruz Biotechnology	Cat# sc-9976; RRID: AB_627502
Anti-p44/42 MAPK (Erk1/2) Rabbit mAb	Cell Signaling Technology	Cat# 4695; RRID: AB_390779
Anti-phospho-p44/42 MAPK (Erk1/2) Rabbit mAb	Cell Signaling Technology	Cat# 4370; RRID: AB_2315112
Anti-DUSP4 (MKP2) Rabbit mAb	Cell Signaling Technology	Cat# 5149; RRID: AB_2750867
Anti-Bim Rabbit mAb	Cell Signaling Technology	Cat# 2933; RRID: AB_1030947
Anti-Bcl-xL Rabbit mAb	Cell Signaling Technology	Cat# 2764; RRID: AB_2228008
Anti-Mcl-1 Rabbit mAb	Cell Signaling Technology	Cat# 94296; RRID: AB_2722740
Anti-phospho-c-Jun (Ser73) Rabbit mAb	Cell Signaling Technology	Cat# 3270; RRID: AB_2129575
Anti-c-Jun Rabbit mAb	Cell Signaling Technology	Cat# 9165; RRID: AB_2130165
Anti-phospho-S6 Ribosomal Protein (Ser235/236) Rabbit mAb	Cell Signaling Technology	Cat# 4858; RRID: AB_916156
Anti-S6 Ribosomal Protein Rabbit mAb	Cell Signaling Technology	Cat# 2217; RRID: AB_331355
Anti-phospho-4E-BP1 (Thr37/46) Rabbit mAb	Cell Signaling Technology	Cat# 9459; RRID: AB_330985
Anti-4E-BP Rabbit mAb	Cell Signaling Technology	Cat# 9644; RRID: AB_2097841
IRDye 800CW Donkey anti-Rabbit IgG	Li-Cor	Cat# 926-32213; RRID: AB_621848
IRDye 800CW Donkey anti-Mouse IgG	Li-Cor	Cat# 926-32212; RRID: AB_621847
IRDye 680LT Donkey anti-Rabbit IgG	Li-Cor	Cat# 926-68023; RRID: AB_10706167
IRDye 680LT Donkey anti-Mouse IgG	Li-Cor	Cat# 926-68022; RRID: AB_10715072
Goat polyclonal anti-rabbit highly cross-adsorbed secondary antibody, Alexa Fluor 568	Life Technologies	Cat# A11036; RRID: AB_10563566
Goat polyclonal anti-mouse highly cross-adsorbed secondary antibody, Alexa Fluor 488	Life Technologies	Cat# A11029; RRID: AB_138404
Bacterial and Virus Strains		
NucLight Red lentivirus reagent (EF1a, Puro) Nuclear-localized mKate2 (Nuc::mKate2)	Essen BioSciences	Cat# 4265
NucLight Red lentivirus reagent (EF1a, Bleo) Nuclear-localized mKate2 (Nuc::mKate2)	Essen BioSciences	Cat# 4627
Chemicals, Peptides, and Recombinant Proteins		
Puromycin	Life Technologies	Cat# A11138-03
Geneticin	Thermo Fisher Scientific	Cat# 11811-031
Blasticidin	Thermo Fisher Scientific	Cat# A1113902
Camptothecin	Selleck Chemicals	Cat# S1288
Vinblastine	Selleck Chemicals	Cat# S1248
Pimasertib	Selleck Chemicals	Cat# S1457
Trametinib	Selleck Chemicals	Cat# S2673
SCH772984	Selleck Chemicals	Cat# S7101
ABT-737	Selleck Chemicals	Cat# S1002
A-1155463	Selleck Chemicals	Cat# S7800
Nutlin-3	Selleck Chemicals	Cat# S1061
S63845	Cayman Chemical Company	Cat# 21131

REAGENT or RESOURCE	SOURCE	IDENTIFIER
Staurosporine	ApexBio	Cat# A8192
N-acetylcysteine	Millipore Sigma	Cat# A8199
Thapsigargin	Millipore Sigma	Cat# T9033
Tunicamycin	Millipore Sigma	Cat# T7765
Paclitaxel	Millipore Sigma	Cat# T7191
JNK Inhibitor VIII	Millipore Sigma	Cat# 420135
2-deoxyglucose	Millipore Sigma	Cat# D8375
Oligomycin	Millipore Sigma	Cat# O4876
Bortezomib	Thermo Fisher Scientific	Cat# NC0587961
Etoposide	Thermo Fisher Scientific	Cat# ICN19391825
MG-132	Thermo Fisher Scientific	Cat# 17-485
Q-VD-OPh	Thermo Fisher Scientific	Cat# OPH00101M
Erastin2 (35MEW28)	Dixon et al., 2014	N/A
Bioactive chemical library (261 compounds)	Selleck Chemicals	Cat# L2000
Cycloheximide	Sigma-Aldrich	Cat# C7698-1G
Polybrene	Sigma-Aldrich	Cat# H9268-5G
Sytox Green	Life Technologies	Cat# S7020
PolyJet	SigmaGen Laboratories	Cat#SL100688
H_2DCFDA	Thermo Fisher Scientific	Cat# D-399
DAPI (4’,6-Diamidino-2-Phenylindole, Dihydrochloride)	Thermo Fisher Scientific	Cat# D1306
FastDigest BstXI	Thermo Fisher Scientific	Cat# FD1024
FastDigest Bpu1120I	Thermo Fisher Scientific	Cat# FD0094
Critical Commercial Assays		
Gateway LR Clonase II Enzyme Mix	Thermo Fisher	Cat# 11791-020
Gibson Assembly Master Mix	New England Biolabs	Cat3 E2611S
QIAshredder RNA Extraction Column Kit	QIAGEN	Cat# 79654
RNeasy Plus RNA Extraction Kit	QIAGEN	Cat# 74134
TaqMan Reverse Transcriptase Kit	TaqMan	Cat# N8080234
QIAprep Spin Miniprep Kit	QIAGEN	Cat# 27106
QIAquick PCR Purification Kit	QIAGEN	Cat# 28106
Q5 Site-Directed Mutagenesis Kit	New England Biolabs	Cat# E0554S
SYBR Green Master Mix	Life Technologies	Cat# 4367659
BCA Protein Assay Kit	Thermo Fisher	Cat# 23225
Deposited Data		
RNA-seq data	GEO	GSE140172
Chemical screening data	Mendeley	https://doi.org/10.17632/9bccjb75wp.1
Experimental Models: Cell Lines		
U-2 OS^N	Forcina et al., 2017	N/A
$T98G^N$	Forcina et al., 2017	N/A
A549	ATCC	CCL-185
$A549^N$	Forcina et al., 2017	N/A

REAGENT or RESOURCE	SOURCE	IDENTIFIER
A549$^{N;\ KTR}$	This paper	N/A
A549$^{N;\ rtTA\text{-}BCL\text{-}xL}$	This paper	N/A
A549$^{N;\ rtTA\text{-}BIM}$	This paper	N/A
A549$^{N;\ rtTA\text{-}BIM\text{-}G156E}$	This paper	N/A
A549$^{N;\ CMV\text{-}Empty}$	Cao et al., 2019	N/A
A549$^{N;\ CMV\text{-}MCL1}$	This paper	N/A
A549$^{N;\ Cas9}$	This paper	N/A
A549$^{N;\ Cas9;\ sgGFP}$	This paper	N/A
A549$^{N;\ Cas9;\ sgMCL1\ \#1}$	This paper	N/A
A549$^{N;\ Cas9;\ sgMCL1\ \#2}$	This paper	N/A
A549$^{N;\ CRISPR\ Control}$	This paper	N/A
A549$^{N;\ MCL1\text{-}LOF1}$	This paper	N/A
A549$^{N;\ MCL1\text{-}LOF2}$	This paper	N/A
Calu-6	ATCC	HTB-56
Calu-6^{N}	This paper	N/A
HEK293T	ATCC	CRL-3216
Oligonucleotides		
See Table S2		N/A
Recombinant DNA		
pLenti CMVTRE3G BCL2L1 Neo	This paper	N/A
pLenti CMVTRE3G BCL2L11 Neo	This paper	N/A
pLenti CMVTRE3G BCL2L11 G156E Neo	This paper	N/A
pLenti CMV MCL1 Puro	This paper	N/A
pMCB306 MCL1 sgRNA #1	This paper	N/A
pMCB306 MCL1 sgRNA #2	This paper	N/A
pLentiCMV Puro DEST ERKKTRClover	Addgene	Cat# 59150
pLentiPGK Puro DEST p38KTRClover	Addgene	Cat# 59152
pLenti CMV rtTA Blast (w756-1)	Addgene	Cat# 26429
pLenti CMVTRE3G eGFP Neo (w821-1)	Addgene	Cat# 27569
pLenti CMV Puro DEST (w118-1)	Addgene	Cat# 17452
pMCB306	Addgene	Cat# 89360
lentiCas9-Blast	Addgene	Cat# 52962
Software and Algorithms		
Prism	GraphPad Software	N/A
Excel	Microsoft Corp.	N/A
FlowJo	FlowJo LLC.	N/A
CellProfiler	Broad Institute	N/A